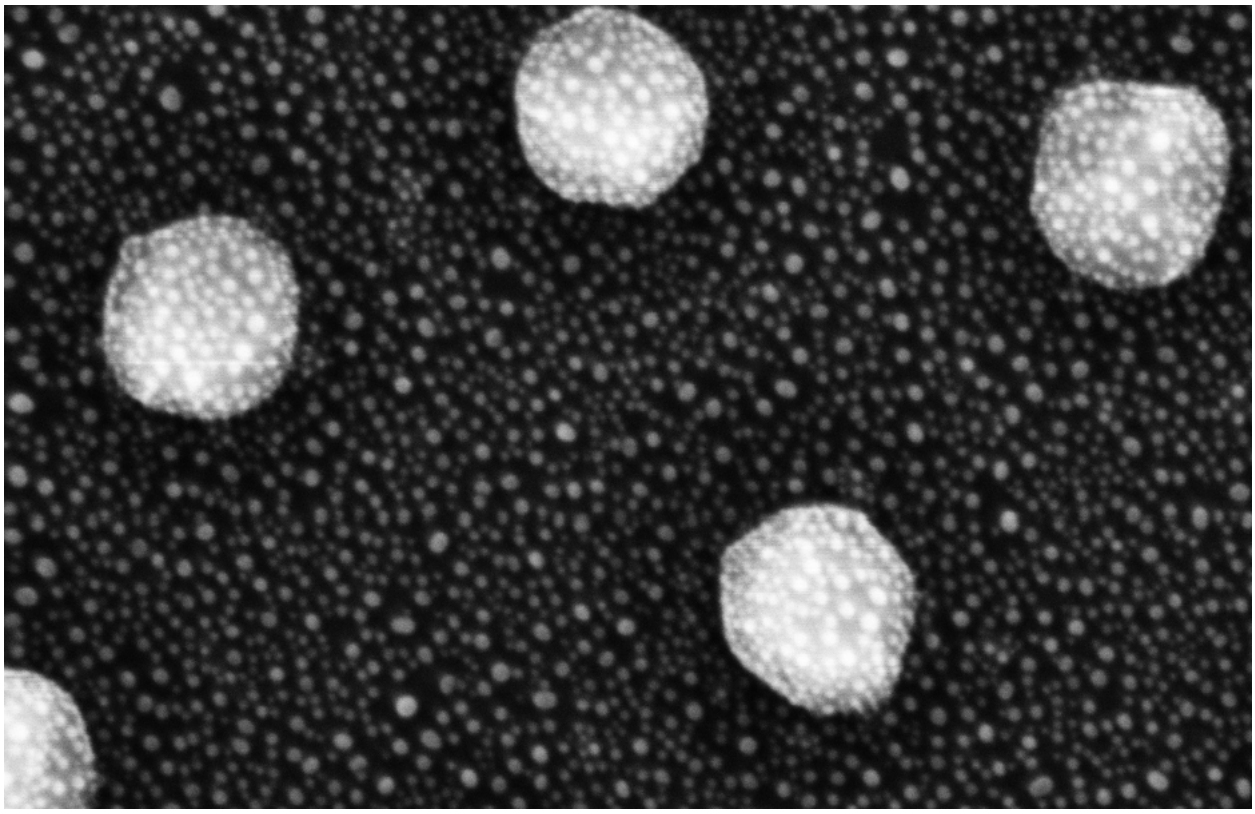

Indirect Nanoplasmonic Hydrogen Sensing

Master's thesis in Physics

RÉMI ALBERT

DEPARTMENT OF PHYSICS

CHALMERS UNIVERSITY OF TECHNOLOGY
Gothenburg, Sweden 2024
www.chalmers.se

Master's thesis 2024

Indirect nanoplasmonic hydrogen sensing

RÉMI ALBERT

CHALMERS
UNIVERSITY OF TECHNOLOGY

Department of Physics
Chemical Physics Division
Chalmers University of Technology
Gothenburg, Sweden 2024

Indirect nanoplasmonic hydrogen sensing
RÉMI ALBERT

Supervisor: Athanasios Theodoridis, Chemical Physics
Examiner: Christoph Langhammer, Chemical Physics

Master's Thesis 2024
Department of Physics
Chemical Physics Division
Chalmers University of Technology
SE-412 96 Gothenburg
Telephone +46 31 772 1000

Cover: Top-view SEM image of Ag nanodisks of $131.6 \pm 5.6nm$ in diameter covered with small Pd nanoparticles $7.06 \pm 3.05nm$.

Typeset in LaTeX from the template created by Kyriaki Antoniadou-Plytaria, used under CC BY 4.0
Printed by Chalmers Reproservice
Gothenburg, Sweden 2024

Indirect Nanoplasmonic Hydrogen Sensors
Rémi Fabrice R Albert
Department of Physics
Chalmers University of Technology

Abstract

The critical role of hydrogen in the global energy transition and its hazardous nature underscores the importance of developing efficient and reliable hydrogen sensing technologies. This thesis explores the advancement of a hydrogen sensing method using indirect Localized Surface Plasmon Resonance (LSPR), where we investigate the alloying properties of small metal nanoparticles by means of solid-state dewetting. The results from this thesis project are divided into three key parts. (i) A proof-of-concept has been realized, showing that indirect LSPR can be used as a means of monitoring hydrogen concentrations, using Ag 140x20nm nanodisks covered with much smaller (few nanometers) hydride-forming Pd nanoparticles. (ii) Building on the insights gathered from the previous part, alloying of $PdAu$ through solid-state dewetting has been investigated to replace the Pd nanoparticles, yielding more than a twofold increase in performance with comparison to (i) and 10 times faster kinetics than its bulk equivalent (i.e. $PdAu$ in direct LSPR). And finally (iii), an attempt to make all depositions through the mask, which proved to be unsuccessful and suggests using a hard sacrificial mask instead of the soft PMMA-based one used in this work. Overall, this thesis highlights the promising potential of indirect LSPR for hydrogen sensing, offering a foundation for future research and technological development in this field.

Keywords: Hydrogen, sensing, sensors, plasmonics.

Acknowledgements

First and foremost, I would like to express my deepest gratitude to my supervisor, Athanasios Theodoridis, Thanos, for his unwavering mentorship and highly dedicated support. Sharing the same office truly enriched my experience, enabling me to clear out any doubt as soon as they showed up.
I also wish to extend my heartfelt thanks to my office mates, Yashna, Sushree and Achilleas for their friendship and support, which greatly enhanced the overall Master's thesis experience. It really added something beyond the mere technological and theoretical learning, I have learned and was inspired by the environment more than in any project before.
Finally, I am thankful to Christoph for his insightful guidance and inspirational character. Being part of this group truly made me feel comfortable.
This thesis could not have been accomplished without such a supportive circle, and I am thankful for every contribution.

Rémi Albert, Gothenburg, June 2024

List of Acronyms

Below is the list of acronyms that have been used throughout this thesis listed in alphabetical order:

AFM	Atomic Force Microscopy
CVD	Chemical Vapor Deposition
EDX	Energy-Dispersive X-ray
EM	Electromagnetic
FIB	Focused Ion Beam
HCL	Hole-Mask Colloidal Lithography
LSPR	Localized Surface Plasmon Resonance
MFC	Mass Flow Controller
PDDA	Poly(diallyldimethylammonium chloride)
PECVD	Plasma-Enhanced Chemical Vapor Deposition
PEMFC	Proton-Exchange Membrane Fuel Cell
PMMA	Polymethyl Methacrylate
POC	Proof-of-Concept
PS	Polystyrene
PVD	Physical Vapor Deposition
QCM	Quartz Crystal Microbalance
SEM	Scanning Electron Microscope
SVR	Surface-area-to-Volume Ratio
TEM	Transmission Electron Microscope

Contents

List of Figures

List of Tables

1
Introduction

The role of hydrogen in the global energy economy is rising quickly. As it is expected to play a pivotal role in decarbonization of industry and in the energy transition [1, 2], it is of utmost importance to ensure a safe and steady development of hydrogen technologies, as hydrogen is hazardous and any incident may cause casualties or at least hinder its deployment. Consequently, fast and reliable monitoring of hydrogen concentrations is critical.

Currently, there exists a vast amount of different techniques to detect hydrogen, including electro-chemical, catalytic, mechanical, acoustic, thermal, resistive and optical [3]. Each method presents unique strengths and weaknesses, but as of today there is not any sensor that has successfully passed all performance benchmarks [4]. Chemiresistive hydrogen sensors are still lagging above $1s$ in response and recovery speed and struggle with sensing low levels of hydrogen. Additionally, their robustness against change happening in their operating environment is not yet demonstrated, regarding poisoning gases, humidity and temperature [5]. The technology of interest in this work falls under the umbrella of optical sensors, specifically nanoplasmonic sensors. These sensors use what is called Localized Surface Plasmon Resonance (LSPR) as a means to detect molecular interactions at the nanoscale and have gathered increasing interest due to their quick response time, high selectivity and potential for poisoning resistance [4].
This project aims to investigate "indirect" plasmonic hydrogen (H_2) sensing [6], leveraging the synergistic benefits of (i) localized surface plasmon resonance (LSPR) and (ii) rapid hydride formation materials. In other words, using chemically inert, yet plasmonically highly active, metal nanoparticles as nanoscopic probes. Ag has been chosen as the ideal candidate for such experiment, as it possesses one of the best plasmonic responses due to its strong and narrow resonance peak. These probes are designed to detect the chemical interactions of H_2 with closely adjacent, much smaller, metallic structures known for their ultra-fast hydride formation, attributed to their high surface-area-to-volume ratio (SVR). An increase in SVR enhances kinetics by accelerating the hydrogen flux and reducing the diffusion path length to the core [4, 7]. These structures will be made using Hole-mask Colloidal Lithography (HCL) [8] and following a recipe proposed by Arturo Susarrey-Arce et al. [9].

The starting experiment is a proof-of-concept (POC), consisting of 140 nm x 20 nm Ag nanodisks protected from oxidation by a thin layer of SiN and covered with very small Pd nanoparticles (a few nanometers). Then, different aspects will be investigated, such as the possibility to use alloyed nanoparticles like $Pd_{70}Au_{30}$ for the

hydride formation, decreasing the hysteresis during the adsorption/desorption and therefore yielding better optical contrast. To do so, we will first start by investigating the de-wetting properties of $PdAu$ alloys on SiN and then attempt to combine it with the POC. A last part of research, as a means to optimize performances, will be to attempt to place the Pd particles solely on the Ag antenna by performing all depositions through the mask, reducing the inactive Pd particles to the bare minimum.

The first part of this project was to nanofabricate such structures in Chalmers' cleanroom facilities at MC2. Then, hydrogen sensing measurements have been performed in the Chemical Physics labs to evaluate the success of the process.

2

Theory

2.1 The role of Hydrogen in modern technology

There are strong reasons to believe that hydrogen will play a major role in the future energy transition, known as the "Hydrogen economy" [1, 2, 10]. This concept aims to solve the energy and climatic crisis by (1) using hydrogen as a universal energy carrier for storing and transporting energy, and (2) decarbonizing areas that currently do not have good low-emission alternatives. Furthermore, its multiple production pathways make it a very strong technology regarding energy safety. It is currently used in several fields, such as metallurgy, agriculture, and chemical manufacturing in the form of, e.g., methanol, ammonia and hydrogen peroxide production [2].

Hydrogen can provide the energy storage to solve the intermittency issue of renewable electricity production, such as wind and solar energy, where the excess electricity produced during peak times can be used to produce hydrogen gas through electrolysis. This stored hydrogen can then be converted back to electricity through the use of fuel cells or synthetic fuels during periods of low renewable electricity production, thus ensuring a stable and reliable base-load electricity supply with low carbon emissions.

Novel applications of hydrogen may allow for decarbonization of the heavy-duty transportation sector using fuel cells or synthetic gas [11], but can also be used in metallurgy as a reducing agent, as exemplified in the process of producing what is called "green steel", steel made with low carbon emission. It is indeed a process that currently generates a lot of carbon emission and does not have many viable options to reduce it except hydrogen [12, 13]. It may also be used in future applications in aerospace and maritime industry, and pharmaceuticals [2].

However, hydrogen can be dangerous if not handled properly. Indeed it has a wide flammability range of 4 $vol\%$ to 78 $vol\%$ in air and one of the lowest minimum ignition energies, at $0.017mJ$ [14]. On top of this, being the smallest element, it is subject to leakages and embrittlement. Ensuring a reliable monitoring of its concentration is of utmost importance.

2.2 Metal Hydride Formation

Hydrogen can form bonds with most elements in the periodic table through covalent, ionic, or hydrogen bonds. Of particular interest in this work is the formation of metal hydrides, where hydrogen bonds with less electronegative elements, such as metals and metalloids, acquiring a partial negative charge. The $Pd - H$ reaction is one of such and is characterized by a high dissociation efficiency, due to a very low activation barrier [15, 16], combined with the ability to absorb monoatomic hydrogen. This combination of great catalytical capabilities and storage medium makes it an excellent candidate for the application of concern in this work. When hydrogen atoms enter the palladium lattice, they induce strain by expanding the lattice, increasing its lattice constant. The different phases are called the alpha (α) and the beta (β) phases and both have different lattice constants [17]. At low hydrogen pressures, we say that the metal particle is in the α phase (Figure 2.1b), which consists of hydrogen atoms entering the lattice without significant $H - H$ interactions, interactions between two hydrogen atoms. As the hydrogen enters the lattice, the strain created slightly increases the lattice constant from 3.887Å to 3.895Å as well as reducing the energy required for another hydrogen atom to take place next to the first one, making it a more favorable location for a new hydrogen atom to take place, which is what we call "H-H interactions". Hydrogen atoms will then start to agglomerate and form larger patches full of hydrogen in the lattice, eventually expanding the lattice parameter further from 3.895Å to 4.025Å. This is the β phase (Figure 2.1d). Following an isotherm, one observes a plateau region during the phase transition, where both α and β phases coexist (Figure 2.1c). This presence of a plateau is necessary to represent a true physical isotherm, forced by the criteria of intrinsic stability $\left(\frac{\partial P}{\partial V}\right)_T < 0$, that is that pressure does not increase with molar volume, and consists of a Maxwell construction. [16, 18]

2.3 Plasmonic resonance

When metal particles are scaled down to sizes comparable to electromagnetic (EM) wavelengths, they exhibit unique optical properties known as localized surface plasmon resonance (LSPR). This phenomenon occurs because the EM field around these nanoparticles is perceived as quasi-homogeneous, causing a coherent displacement of the electron cloud relative to the metal's positive nuclei. This displacement creates a charge separation within the particle, which in turn generates a restoring force due to Coulomb attraction that brings back the electrons toward the nucleus. If the frequency is correct, restoring force and EM field can be in phase coherence, resulting in a resonant phenomenon known as *Localized surface plasmon resonance* (LSPR). This particular frequency is called *plasmon frequency* and depends on the density of electrons, the effective electron mass, and the shape and size of the charge distribution, as well as the optical properties of the surrounding medium. The density of electrons and the effective electron mass dependent on the material, but size and shapes can be modified at will without great difficulty with current nanolithography techniques. For instance, Au nanospheres can be placed in colloidal solution

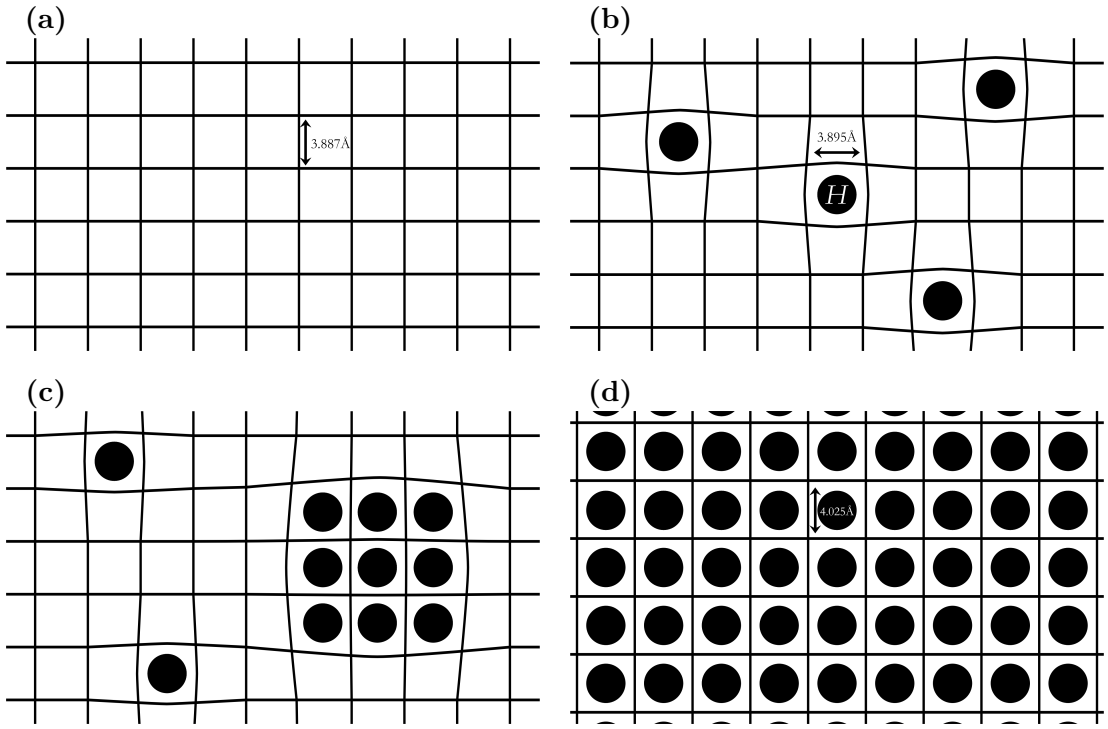

Figure 2.1: Visual representation of hydrogen atoms entering the metal lattice with increasing hydrogen pressure.
(a): No hydrogen, lattice constant is 3.887Å
(b): Hydrogen atoms start to enter the metal lattice, locally straining it around the hydrogen atoms. Lattice constant is expanded to 3.895Å
(c): As hydrogen pressure increases, H-H interactions start to occur and beta phase areas appear.
(d): Once all hydrogen atoms have taken their place in the lattice, the hydride is fully formed and the lattice has been expanded, increasing its lattice constant. For instance, *Pd* lattice constant expands from 3.895Å to 4.025Å.

to change the liquid color depending on their sizes, as shown in Figure 2.2.

Figure 2.2: Colloidal dispersion of gold nanoparticles in water, displaying varied colors due to their size-dependent plasmonic resonance. [19]

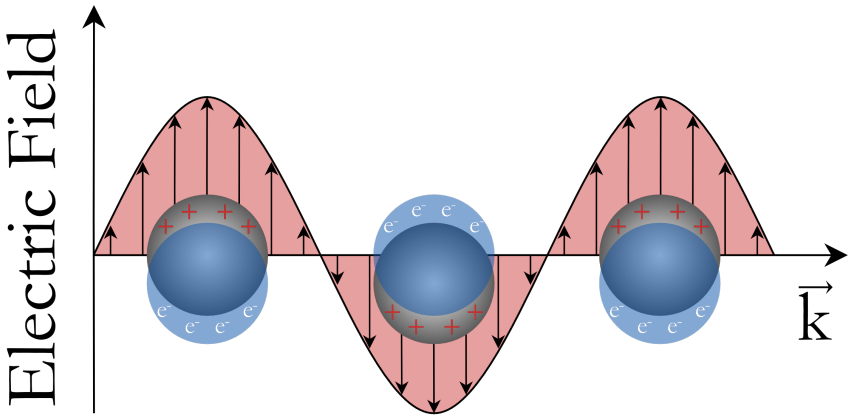

Figure 2.3: Schematic of plasmon oscillations for nanospheres, showing the charge separation generated by the coherent displacement of the electron cloud (blue) relative to the particle's center (grey). Red plus signs and white e^- respectively represent fictive positive and negative charges.

There are multiple modes of plasmon excitation, the simplest being the *dipole plasmon resonance*, where the collective oscillation of electrons resembles a simple dipole. Higher-order modes, such as the *quadrupole mode*, involve more complex patterns of charge distribution and can lead to different optical behaviors, but often have negligible impacts in very small particles, such as these considered in this work.

Since Mie's 1908 paper providing a solution to Maxwell's equations describing the extinction spectra of spherical particles of arbitrary size [20], it is possible to predict

with high precision the behavior of such particles under light exposure. However, these can become a bit complicated but fortunately for small particles, it is easy to relate the dipole plasmon frequency of a metal nanoparticle to its dielectric constant using some clever approximations. To do so, one can use the quasistatic approximation, where the electric field is taken as constant and the problem to be solved shifts from electrodynamics to electrostatics, simplifying significantly the derivations. Under these circumstances, one finds the extinction and scattering efficiencies to be

$$Q_{ext} = 4xIm(g_d) \tag{2.1}$$

$$Q_{sca} = \frac{8}{3}x^4|g_d|^2 \tag{2.2}$$

where $g_d = \frac{\epsilon_i - \epsilon_0}{\epsilon_i + 2\epsilon_0}$ and $x = 2\pi a(\epsilon_0)^{1/2}/\lambda$, with ϵ_i and ϵ_0 being the dielectric constants of the nanoparticle and surrounding medium, respectively. λ is the wavelength of the incident light, and a the particle radius.

2.4 Direct and Indirect LSPR Hydrogen sensing

LSPR can be exploited as a means of spectroscopic characterization, providing an attractive sensing method for its sensitivity and versatility [21]. LSPR hydrogen sensing can be direct [22] or indirect[6], the difference being the location of the hydrogenation. In the first case, the hydrogenation occurs in the plasmonically active nanoparticle that will be monitored, which is typically made of a hydride-forming material, with the most common being Palladium (Pd). When hydrogen is absorbed into the metal lattice, the particle undergoes changes in its electronic and optical properties. In the case of Pd, this change consists of two phases called α and β, depending on the hydrogen concentration as shown in Figure 2.1 This absorption affects the particle's dielectric constant, causing a shift in its LSPR signal.

Direct sensing provides high sensitivity and specificity due to the inherent affinity of the hydride-forming material for hydrogen. For example, palladium nanoparticles can detect hydrogen concentrations at the ppm level [4]. However, direct sensing often suffers from issues such as hysteresis, a difference in hydrogen pressures during absorption and desorption, leading to an ambiguous readout as the response depends on sensor history. In the case of Pd, this is due to the fact that direct sensing requires larger particles to position the plasmon peak in the visible regime, as well as increasing optical contrast. It can, however, be solved by alloying the Pd with, for instance, gold [23]. On the other hand, it is also possible to use such a particle as an antenna that senses changes in the surrounding medium. Here, the nanoparticle itself does not undergo hydrogenation. Instead, a secondary hydride-forming material surrounds the highly plasmonically active nanoparticle and is responsible for hydrogen reaction. Since it is the change in the environment and not directly in the primary particle that is monitored, it is called "Indirect sensing". By tailoring the secondary material's properties, one can design sensors with enhanced selectivity and response times [6]. An illustration of these two methods is depicted in Figure 2.4.

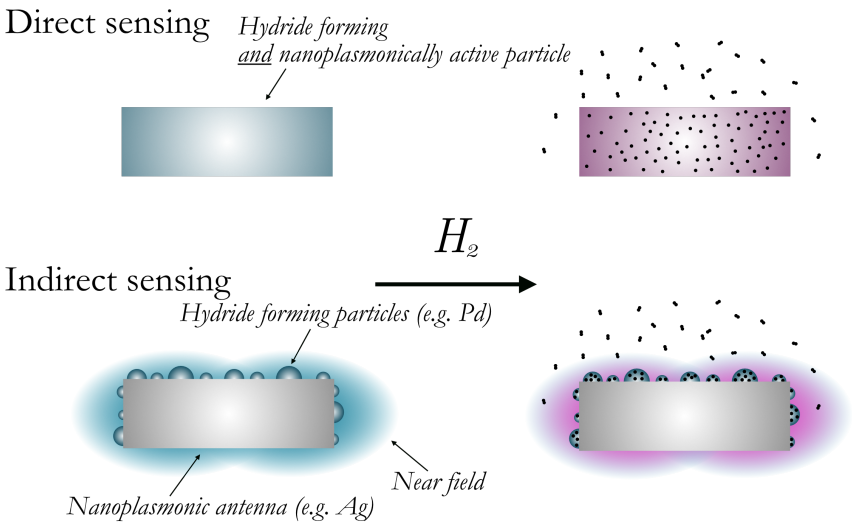

Figure 2.4: Artistic representation illustrating the difference between direct and indirect LSPR hydrogen sensing. In the direct case (top), the particle undergoing hydride formation is also the nanoplasmonically active particle, with a color change representing the shift in peak resonance. This particle can be made of Pd or Pt for instance. On the other hand, the indirect method (bottom) separates the two phenomena. The nanoplasmonically active particle does not undergo hydrogenation and instead simply acts as an inert antenna, sensing change in its environment with its near field. Smaller hydride-forming particles alter the local environment of the antenna, therefore influencing its optical response.

3

Nanofabrication Processes & Characterization Methods

The main fabrication process follows a recipe taken from Arturo Susarrey-Arce et al. [9] and is presented in Figure 3.1. Initially, the Hole-mask Colloidal Lithography (HCL) is used only to produce the amorphous array of silver nanoparticles (140 nm x 20 nm), and in a second time, it will be kept until the very end, after the Pd deposition. The SiN protective layer is deposited through Reactive sputtering or Plasma-Enhanced Chemical Vapor Deposition (PECVD). We will see later that this is a critical part in the process and has significant impacts on the measurements. Finally, the small Pd and $PdAu$ nanoparticles are produced through dewetting of thin films, ranging from 1Å to 15Å. If there is need to be imaged, the process is done simultaneously on SiO_2 and Si chips, the later being suitable for SEM imaging as it is conductive, which SiO_2 is not. Afterward, the hydrogenation measurements are carried out in the atmospheric pressure flow reactor Insplorion $X1$.

3.1 Hole-Mask Colloidal Lithography

The Hole-Mask Colloidal Lithography method is an ingenious process resulting in a quasi-ordered amorphous array of nano-holes used as waste, which can in turn be used to produce a series of nanostructures (disks, dimers, ...). The version used in this work is presented in Figure 3.1.

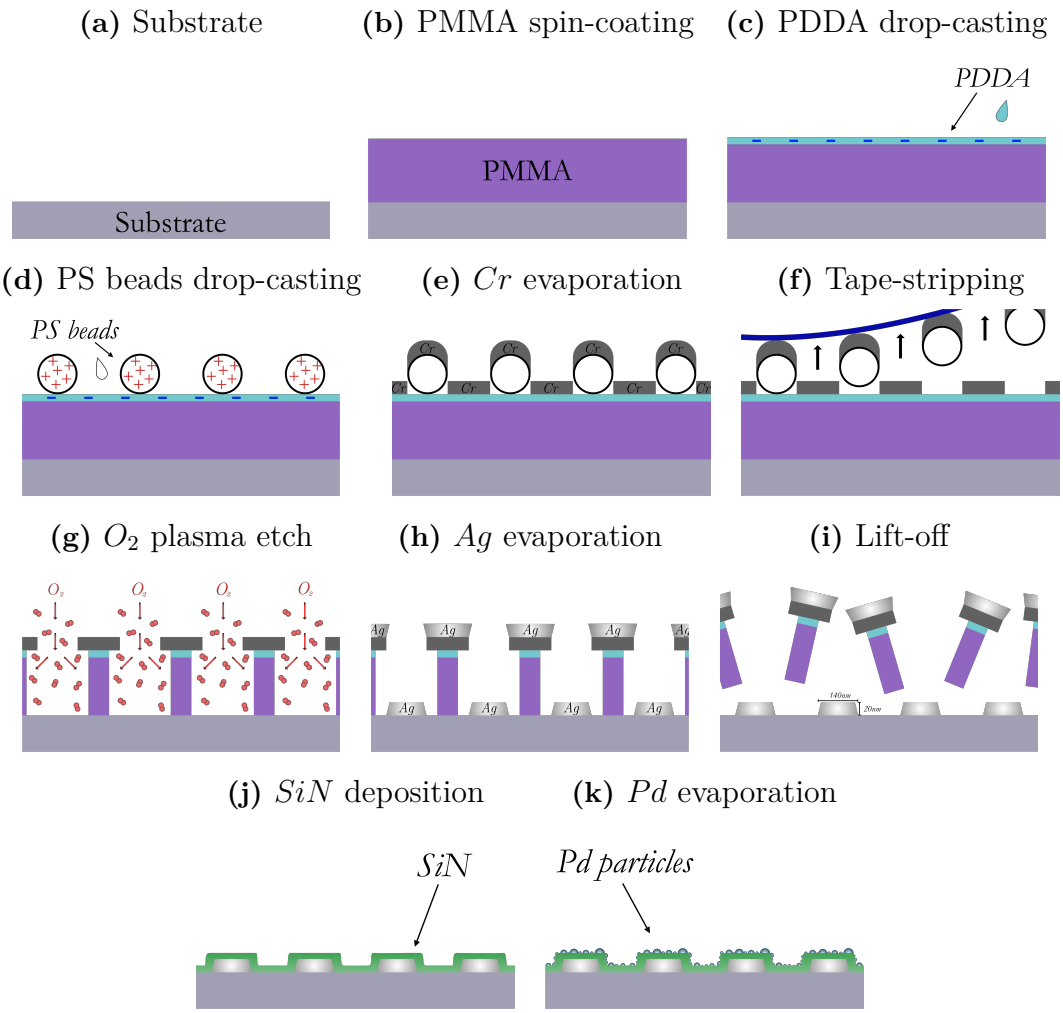

Figure 3.1: Step by step schematics of the nanofabrication process.
(a): The substrate is either composed of SiO_2 if the sample is intended to be used for hydrogenation measurement, or with fused silica (Si) for SEM imaging. It was cleaned for $5min$ in Acetone and IPA with sonicator before.
(b): Spin-coating of the PMMA sacrificial layer on the substrate.
(c): drop-casting of the negatively charged PDDA layer. Blue minus signs (-) indicate fictive negative charges.
(d): drop-casting of the positively charged PS beads. Red plus signs (+) indicate fictive positive charges.
(e): 200 nm Cr evaporation on top of the PS beads.
(f): Tape-striping of the PS beads, revealing an amorphous array of nanoholes the size the beads (140x20 nm).
(g): Oxygen plasma etching through the holes. Notice the under-etch larger than the holes as the plasma penetrates inside.
(h): $20nm$ Ag evaporation. Notice the shrinking of the hole during the deposition, effectively depositing a cone-like structure more than a disk.
(i): Lift-off of the mask, leaving an amorphous array of 140 x 20 nm Ag nanodisks.
(j): SiN protective layer deposition through reactive sputtering or PECVD. Notice the better step coverage than for evaporation, which is especially true for PECVD.
(k): Pd nanoparticles formation through dewetting of thin film. The thin Pd film is evaporated and then annealed to enhance the dewetting phenomenon.

3.1.1 PMMA

The first step of the process is to deposit the PMMA sacrificial layer (Figure 3.1b). It will be used as a basis to build the mask, as it is easy to remove with solvents afterward. The deposition is done through spin-coating of PMMA 95⌀ A4 at 2000 rpm for $60s$, resulting in a film of approximately 200 nm. It is then soft-baked at $170°C$ for $3min$ to evaporate any solvent leftover. Spin-coating enables easy and uniform deposition of thin layers by utilizing the centrifugal force arising from high-speed rotation. The thickness of the deposited layer can be controlled by increasing or decreasing the angular speed and the rotation time; a higher speed results in a thinner layer. Following this deposition, the PMMA layer is exposed to a short $5s$ of O_2 plasma etch at $50W$ to make the surface more hydrophilic, which helps for the next step: drop-casting.

3.1.2 Drop-casting

Drop-casting was employed to first deposit a positively-charged PDDA film onto the PMMA (Figure 3.1c), followed by a colloidal dispersion of negatively charged polystyrene (PS) beads with a diameter of 140 nm (Figure 3.1d). The reason for these electric charge is twofold. First, the difference in electric charge between the PDDA and the PS beads ensures that the beads stick to the surface throughout the whole process. Then, the Coulombic interactions between the beads allow for a consistent method to control the spacing between the beads, ensuring uniform distribution. This method results in a quasi-ordered layer of PS beads, which is crucial for the following steps.

PDDA Deposition (0.2 *wt.% in water*):

1. PDDA was drop-casted onto the chip for a duration of at least 1 minute to ensure adequate adsorption and reached saturation.
2. The chip was then rinsed under a trickle of water for a few seconds to remove excess PDDA.
3. After rinsing, the chip was vertically blow-dried to ensure uniform evaporation of the water from the center outward, resulting in the formation of a thin layer of PDDA.

PS Bead Deposition (140 nm⌀):

1. The PS beads were deposited in a similar manner, allowing 2 minutes for bead adsorption before rinsing.
2. The critical drying step involved carefully blow-drying the chip to avoid dislodging the beads. Care was taken to prevent any water droplets from returning to the top of the chip after drying, as this could rinse away the beads.

3.1.3 Cr and Ag evaporation

Once the PS beads are disposed on the surface, 20 nm of Cr are evaporated on top of it (Figure 3.1e). The samples are then *tape-stripped*, effectively removing the

PS beads from the surface (Figure 3.1f). This leaves a Cr mask filled with nanoholes where the sacrificial layer is exposed. The tape-stripping should be performed carefully to ensure that the Cr layer remains intact around the holes and that no residues of PS beads are left on the surface. Following this, the sample is exposed to O_2 plasma at $50W$ for $5min$ to etch through these holes all the way down to the substrate (Figure 3.1g). The hole-mask is now ready and Ag particles can be evaporated through these holes in a similar manner as for the Cr(Figure 3.1h).

In the first case, the mask is lifted-off once the Ag particle have been evaporated (Figure 3.1i). Later, all deposition, including the SiN and the $Pd/PdAu$, will be deposited through the mask before lift-off.

3.1.4 Protective layer: SiN

The protective layer, crucial for preventing the Ag particles from oxidizing, is composed of a thin layer of SiN ranging from 3.5 to 14 nm depending on the measurement. It has first been deposited using reactive sputtering, at a rate of 0.175 nm/s and later with PECVD (Figure 3.1j) using the available recipe combining low and high frequency depositions to achieve a low stress thin film. Each cycle nominally deposits 5.58 nm of SiN.

3.1.5 Nanoparticle formation

The last step of the nanofabrication is the formation of the small $Pd/PdAu$ nanoparticles (Figure 3.1k), which has been done through solid-state dewetting.

Dewetting of liquid films is a spontaneous process that is quite well understood. It is commonly observed in solid–liquid interfaces, such as when a water film on a glass window slowly reduces into droplets. This phenomenon is driven by surface free-energy minimization and kinetically mediated by the hydrodynamics of the liquid.

A less intuitive phenomenon occurs when solid metallic films are reduced to very small thicknesses, such as a few Ångströms, and heated up, even below melting point. One can then observe what is called *solid-state* dewetting: a spontaneous agglomeration of the solid thin film into an assembly of 3D crystallites [24]. Although solid-state dewetting is less understood than liquid state dewetting, it can be used to produced nanoparticles of diameter lying in the nanometer range [25]. Nanoparticle sizes are influenced by (i) Annealing temperature, (ii) annealing time, and (iii) deposited thickness. A representation of the process is shown in Figure 3.2.

For the alloying of $PdAu$ nanoparticles, the two layers have been deposited on top of each other with varying nominal thicknesses maintaining a relative composition of 30% Gold and 70% Palladium. This composition has previously been found to be optimal for reducing hysteresis while maintaining good sensitivity of plasmonic H_2 sensors [26].

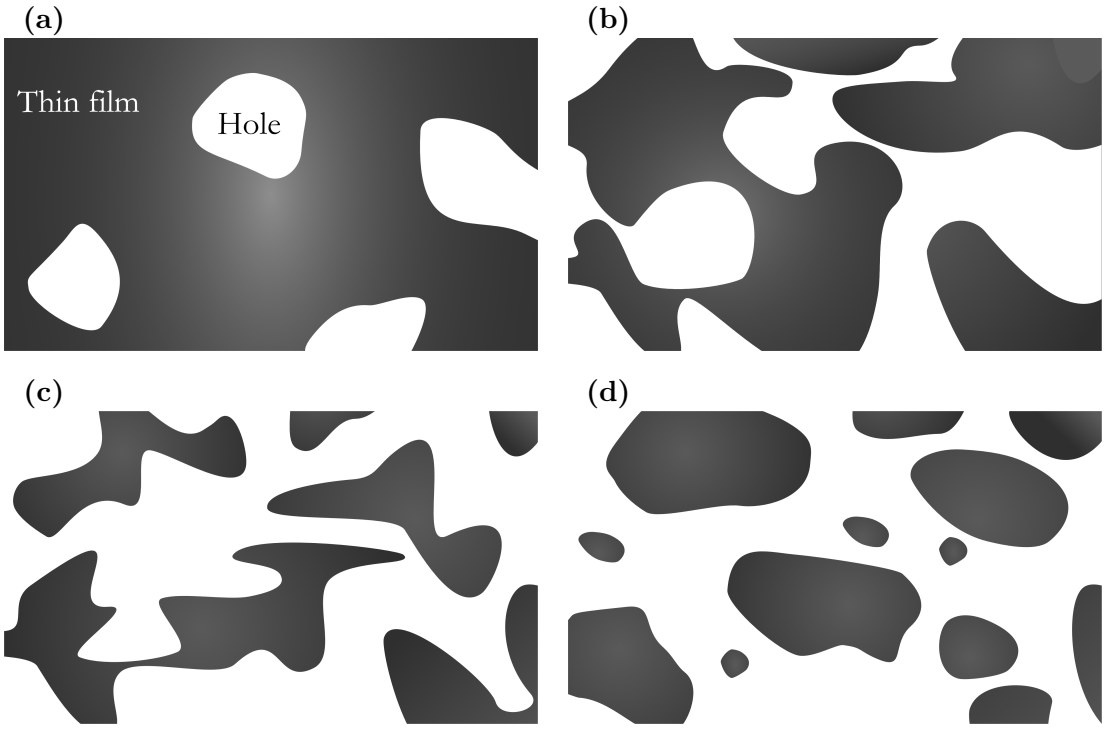

Figure 3.2: Artistic representation of nanoparticle formation through solid-state dewetting. The initial situation (a) is that of an inhomogeneous thin films, composed of hole areas. Holes then start to expand (b) and material agglomerates (c). After some time, the nanoparticles are formed (d). Nanoparticle sizes are influenced by (i) Annealing temperature, (ii) annealing time, and (iii) deposited thickness.

3.2 Thin film deposition

There are several ways of depositing thin films on a sample. The methods used in this work are Physical Vapor Deposition (PVD), in the form of reactive sputtering and evaporation, Chemical Vapor Deposition (CVD), spin-coating and drop-casting. PVD is a type of thin film deposition which uses solid or liquid precursors, as opposed to CVD, which uses gases. There are several ways of achieving PVD, but all relies on the ejection of a specific material from a target through a high vacuum onto the substrate surface where the film is to be deposited. Means of ejecting these atoms include resistive heating, electron beam heating, ion bombardment, or laser beam bombardment.

3.2.1 Evaporation

Evaporation is a natural phenomenon occurring at the interface of a solid or liquid phase with a gaseous phase, where the latter condenses and forms a thin film onto the former. This phenomenon is further increased by greater vapor pressures of the considered material. One such way of increasing the vapor pressure of a given material is to heat it up, which is usually achieved through resistive or electron beam heating. Hot metals have high vapor pressures in high vacuum and atoms are

transported to the substrate in this way. Evaporation in this work has been achieved using a Lesker PVD 225 e-beam evaporator. It consists of a high-energy electron beam that is manipulated with a magnetic field to hit and heat the target, which is composed of the metal that is wished to be deposited. The rate of deposition and the deposited film thickness is monitored by sensing the mass variation of the deposited film using a Quartz Crystal Microbalance (QCM).

3.2.2 Reactive sputtering

Sputtering is a vacuum process that consists in bombarding a target source material with ions, ejecting atoms from it towards the substrate. Traditional sputtering typically occurs in an inert gas plasma such as argon, where the ejected atoms travel all the way to the substrate without chemical reaction. Alternatively, one can use so-called *reactive sputtering*, which is a variant of traditional sputtering, where sputtering occurs in a reactive gas atmosphere, such as O_2 or N_2. The atoms leaving the target will then react with the surrounding ionized gas as they travel from the target to the substrate and form a new compound, which then deposits on the substrate. This is what has been used to produce SiN in the first time, before moving on to *PECVD*.

3.2.3 PECVD

Plasma-enhanced chemical vapor deposition (PECVD) is a type of chemical vapor deposition making use of ionized gas (plasma) to deposit a thin solid film onto a substrate. The plasma is generated by radio frequency (RF) or direct current (DC) discharges. Atoms, or more complex molecules, from different reactants adsorb on the surface and collide to form the combined compound. In order to produce silicon nitride (Si_3N_4), silane (SiN_4) and ammonia (NH_3) can be combined. PECVD is characterized by an excellent step coverage in comparison to evaporation and sputtering, the ability to uniformly cover the substrate surface regardless of its topography, which is due to the fact that gases can diffuse into crevices, around corners, and onto all surfaces, leading to a more uniform film deposition even on complex topographies, as opposed to the "line-of-sight" trajectory of PVD techniques.

3.3 Experimental setup

3.3.1 X1 Reactor

The main reactor used for the hydrogen measurements is a quartz tube flow reactor (Insplorion X1). It has an effective volume of approximately $190mL$ and allows for the simultaneous optical monitoring of two sensor chips at a time. It is wrapped in a resistive heating coil to allow for temperature monitoring and control during the experiment using a thermocouple as a feedback-loop. Mass Flow Controllers (MFC) are used to precisely control the gas mixture injected into the reactor at atmospheric pressure. The spectrometry measurements following the resonance peak

of the samples (Ag/Pd and $Ag/PdAu$) are carried out using the M8 software from Insplorion AB.

3.3.2 Gas protocols

Different gas protocols have been used throughout this thesis.
The final gas protocol consists of a primary heating step at 120°C to get rid of the water molecules present on the surface of the samples and in the chamber. It is then followed by 5 strong H_2 pulses at 10 $vol\%$ to initialize the surface.
The sensing measurements consists of 10 pyramidal H_2 pulses ranging from 0.06 to 1.26 $vol\%$ in Argon. Three different temperatures have been investigated; 30°C, 50°C and 80°C.

3.4 Spectral characterization

In LSPR, one can monitor different features such as the resonant peak position, the intensity or the centroid (center of mass) of the peak, the latter exhibiting a superior signal-to-noise ratio [27, 28]; this is the one that will be used in this work. Figure 3.3 depicts these different quantities.

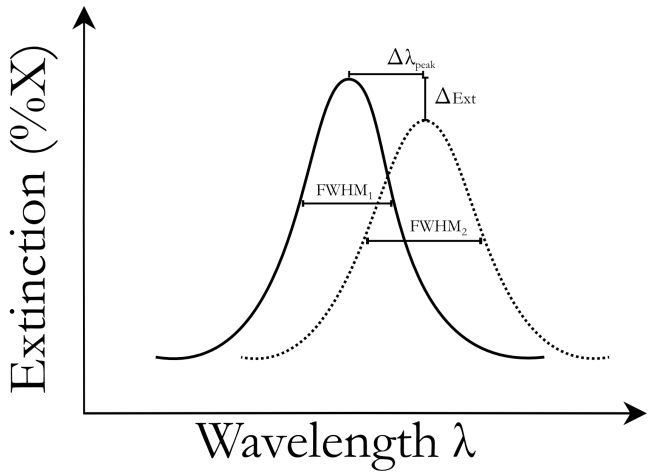

Figure 3.3: Schematic of the different properties that can change and be tracked in the optical response during a LSPR measurement. One option is to monitor the change in peak position $\Delta\lambda_{peak}$, but one can also track the change in peak intensity ΔExt, and the variation of Full Width at Half Maximum (FWHM), indicating the widening or narrowing of the peak.

3.4.1 Interpolated tracking centroid algorithm

The technique used to monitor the optical change under introduction of H_2 gas in the chamber is called *Interpolated tracking centroid* [27, 28] and is a more advanced method of tracking variations in peak position than simply looking at the maximum

value.

The algorithm starts by asking for a "guess" of the peak position λ_{guess}, where we expect the peak to lie, and a span S. The span is the width of the peak we want to analyze. From there, we define λ_s as $\lambda_{guess} - S/2$, i.e., the leftmost point of the peak. Then, the centroid, or the center of mass, of the peak is obtained by calculating the first moment of the function defined by $f(\lambda, t) = \epsilon_{fit}(\lambda, t) - \epsilon_{base}$, where ϵ_{fit} is a high order polynomial fit of the data given by Eq. 3.1 and $\epsilon_{base} = \epsilon_{fit}(\lambda_s) = \epsilon(\lambda_s + S)$, or, in other words ϵ_{base} is the lowest value at which we start to analyze the peak. This function essentially isolates the peak in the chosen interval.

$$\epsilon_{fit}(\lambda, t) = \sum_{i=0}^{n} p_{i+1} \lambda^i \tag{3.1}$$

The centroid $\lambda_{centroid}$ is then calculated using

$$\lambda_{centroid}(t) = \frac{\int_{\lambda_s}^{\lambda_s+S} \lambda \left(\epsilon_{fit}(\lambda, t) - \epsilon_{base}\right) \mathrm{d}\lambda}{\int_{\lambda_s}^{\lambda_s+S} \left(\epsilon_{fit}(\lambda, t) - \epsilon_{base}\right) \mathrm{d}\lambda} \tag{3.2}$$

$$= \frac{Numerator}{Denominator} \cdot \sigma_\lambda + \bar{\lambda} \tag{3.3}$$

where

$$Numerator = \sum_{i=0}^{n} \left[\frac{p_{i+1}}{i+2} \left(\left(\frac{\lambda_s + S - \bar{\lambda}}{\sigma_\lambda} \right)^{i+2} - \left(\frac{\lambda_s - \bar{\lambda}}{\sigma_\lambda} \right)^{i+2} \right) \right] - \frac{\epsilon_{base} \cdot S}{2} \cdot \left(\frac{\lambda_s + S - \bar{\lambda}}{\sigma_\lambda} \right)^2 - \left(\frac{\lambda_s - \bar{\lambda}}{\sigma_\lambda} \right)^2 \tag{3.4}$$

$$Denominator = \sum_{i=0}^{n} \left[\frac{p_{i+1}}{i+1} \left(\left(\frac{\lambda_s + S - \bar{\lambda}}{\sigma_\lambda} \right)^{i+1} - \left(\frac{\lambda_s - \bar{\lambda}}{\sigma_\lambda} \right)^{i+1} \right) \right] - \epsilon_{base} \cdot \frac{S}{\sigma_\lambda} \tag{3.5}$$

where n is the degree of the polynomial and p_i is the coefficient of the i_{th} order. It has been shown that polynomial degrees above $n = 20$ do not improve results [27], hence this is the degree that has been used in this work. $\bar{\lambda}$ is the mean wavelength value and σ_λ is its standard deviation, they are present because the Matlab function used to fit the polynomial, *polyfit*, centers and scales the values as $\hat{x} = \frac{x - \bar{x}}{\sigma_x}$. This ensures that we regenerate spectral data.

3.4.2 Pulse Shift Extraction

To extract the centroid shift, the datapoints are first baseline corrected by linearly interpolating the data before and after the pulse, to simulate as if there had not been any pulse. This help account for the small drift that naturally occurs during measurements. Once this has been done, the datapoints are averaged during the pulse, with a dead time of 20s, which gives the value of the centroid shifts since the

datapoints have been baseline corrected. An example of such correction is shown in Figure 3.4.

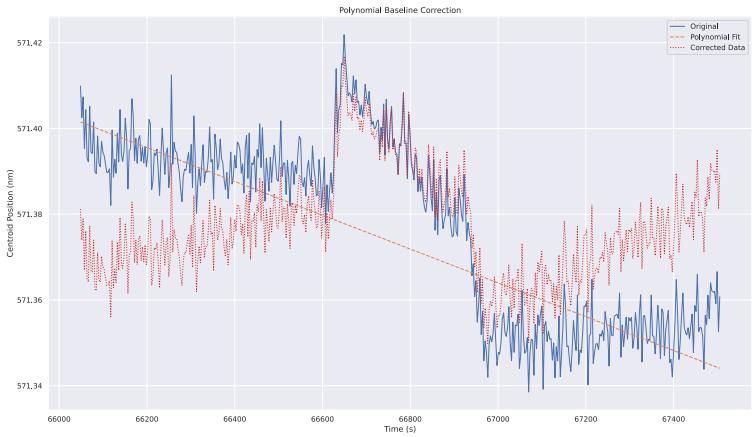

Figure 3.4: Example of baseline correction for the peak shift

3.4.3 Particle Size Measurement

The quantity used to evaluate the size of all particles is called the *feret diameter* [29]. It is defined as the distance between two parallel tangential lines of a randomly oriented particle and can be used to determine the particle's perimeter, if the particle is concave, following Cauchy's second theorem [30]:

$$\langle D_f \rangle = P/\pi \tag{3.6}$$

Particle size statistics can be measured using the software *ImageJ*. The method used to measure the size of the particle works by finding a way to apply a mask on each particle, the size of this mask will then be evaluated by its size in pixels, which has been calibrated with the scale bar available in the bottom of the image. There are different ways of pre-processing the image to make it suitable for particle measurement, the one used in this work is as follows:

1. Adjust the brightness and contrast to make the particles stand out as much as possible, without loosing particles or blurring the image.
2. Make the image binary, i.e., purely black and white.
3. Apply binary median filter to remove edge noise and smooth out the particles.
4. Manually cut out overlaps if needed.
5. Dilate or erode the particle while comparing with the original image to fit with the initial particles as much as possible.
6. Analyze particles from the Analyze tab.

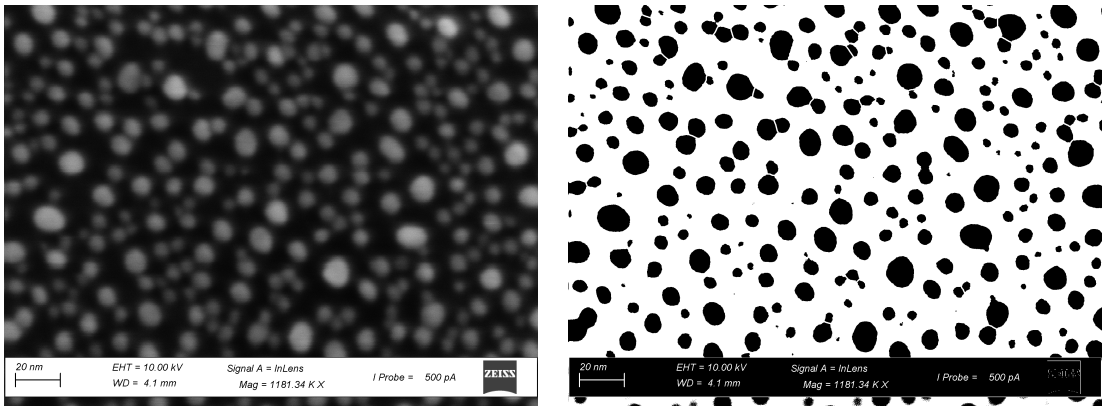

(a) **(b)**

Figure 3.5: Side by side comparison of a top-view SEM image with *Pd* nanoparticles pre- (a) and post- (b) processing in ImageJ for particle size analysis.

4

Results

4.1 Proof-of-Concept

The first objective was to produce a proof-of-concept (POC), showing that this technique is indeed usable for hydrogen measurements. This section will present the different steps and considerations involved in fabricating such device, notably the SiN protective layer thickness and deposition method, and the influence of Pd nanoparticle size. A last part is left for investigating the hydrogenation kinetics.

4.1.1 Influence of SiN deposition

A major issue with using Ag is its propensity at forming oxides. If left exposed to ambient air, its plasmonic response quickly degrades over time, which is why it is usually protected by a thin layer of, for instance, SiN or SiO_2[31, 32]. Therefore as a primary experiment, samples with different thicknesses of SiN have been exposed to gradually increasing O_2 plasma etching as a means to assess their protectivity potential and decide upon which thickness would be sufficient for the following experiments. The harsh conditions of O_2 plasma allow for the emulation of a long exposition to ambient air. One can see in Figure 4.1 that after high O_2 plasma exposition, the two samples with thinner layers, (4.1a) and (4.1b), have been destroyed while the two thicker (4.1c) and (4.1d) ones remained operational, albeit weaker. Thus a thickness of around 10.5 mn, has been deemed sufficient to protect the sensor from ambient oxidation.

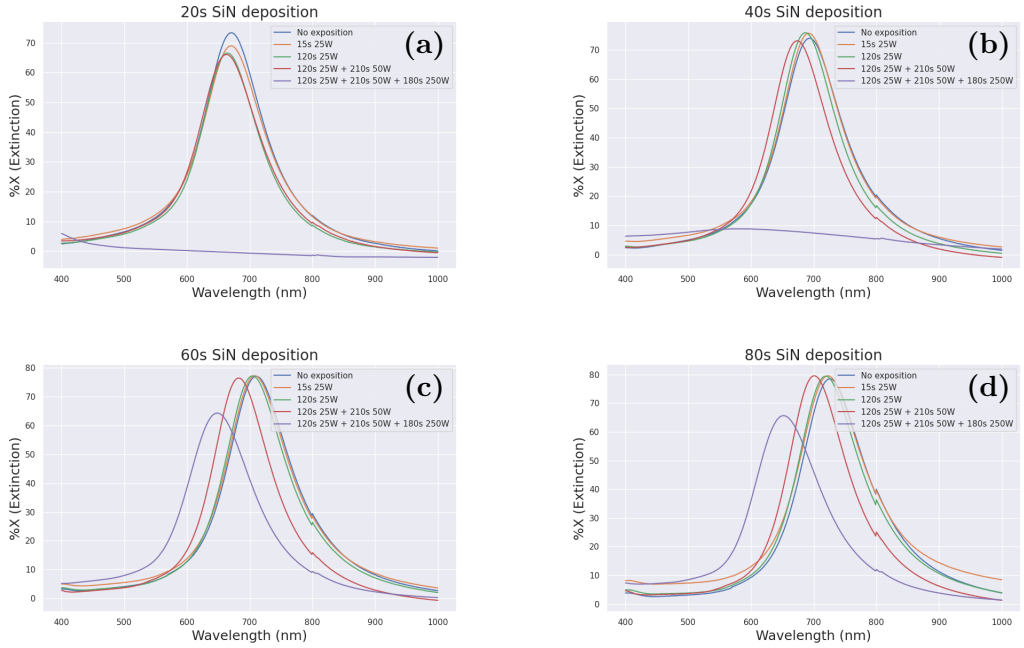

Figure 4.1: Comparison of the resistivity against O_2 plasma of different sputtered SiN thicknesses (a): 20s (3.5 nm), (b): 40s (7 nm), (c): 60s (10.5 nm), (d): 80s (14 nm). The graphs show the extinction % for wavelength ranging from 400nm to 1000nm after different O_2 plasma exposition times and power. We can see that for the strongest exposition (purple), the two thin layers (a) and (b) became unusable while the two thicker layers (c) and (d) remained operational, albeit less efficient.

The quality of the protective SiN layer has had a significant impact on the results. A primary observation is that, for the purpose of this experiment, the sputtered SiN failed to provide a sufficient quality film, as they exhibited a hydrogen response even in the absence of active components. For this reason, $PECVD$ had to be used instead due to its ability to produce higher quality SiN films. Figure 4.2 compares hydrogenation measurements of two blank samples, composed only of the amorphous array of Ag nanoparticles and the different SiN layers, i.e., no Pd nanoparticles. It can clearly be seen that the sample made using Sputtered SiN does not behave in a desirable manner. The sample reacts to hydrogen pulses, despite not having active components (Pd nanoparticles) and, furthermore, the reaction is irreversible; the response is asymmetrical around the pyramid pulse.

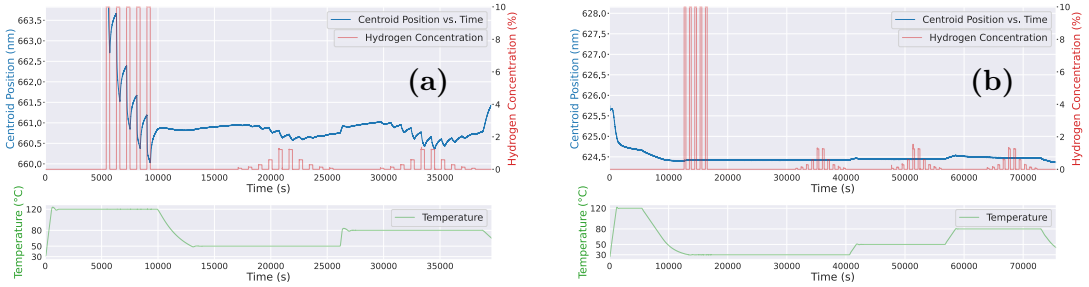

Figure 4.2: Comparison of the effect of (a) sputtered SiN versus (b) PECVD SiN on blank samples (without Pd nanoparticles). The centroid position is reported in blue on the left y-axis, and hydrogen concentration is following the right y-axis in red. Below the main graph is the corresponding temperature at each time step.

This unwanted response scales with temperature and renders the sensor unreadable at higher temperature, if not already causing inconsistencies even at low temperature. Figure 4.3. illustrates this erratic behavior, particularly at elevated temperatures where the sensor completely misbehaves and to some extent also at room temperature. The sample is composed of a nominal $40s(7\ nm)$ of sputtered SiN and 5 Å of Pd.

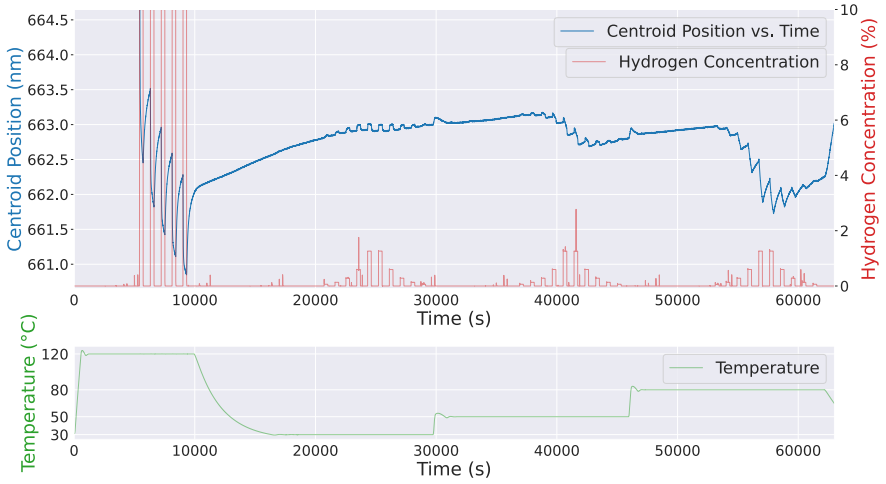

Figure 4.3: Example of bad SiN behavior at higher temperature. The sample is composed of $40s(7\ nm)$ of Sputtered SiN and 5 Å of Pd. Unusual spikes in hydrogen concentrations come from interference of the MFCs with other measurements in the lab but do not affect the measurements.

Now using $PECVD\ SiN$, we can observe the influence of the thickness of the protective layer. The new measurements are made with three different thicknesses, corresponding to 1 (thin), 2 (intermediate) and 3 (thick) cycles of the low stress MF SiN PECVD recipe available at MC2. A recipe working as a combination of LF and HF depositions applied successively in cycles. Each cycle nominally produces a thin 5.6 nm SiN layer with low stress. We have observed two major phenomena:

First, a too thin SiN layer fails to protect the sensor from baseline drifts due to temperature. As shown in Figure 4.4, measurements at low temperature (a) are satisfactory, but as temperature increases to (b) 50°C and (c) 80°C, the thinner layers start to irreversibly blueshift.

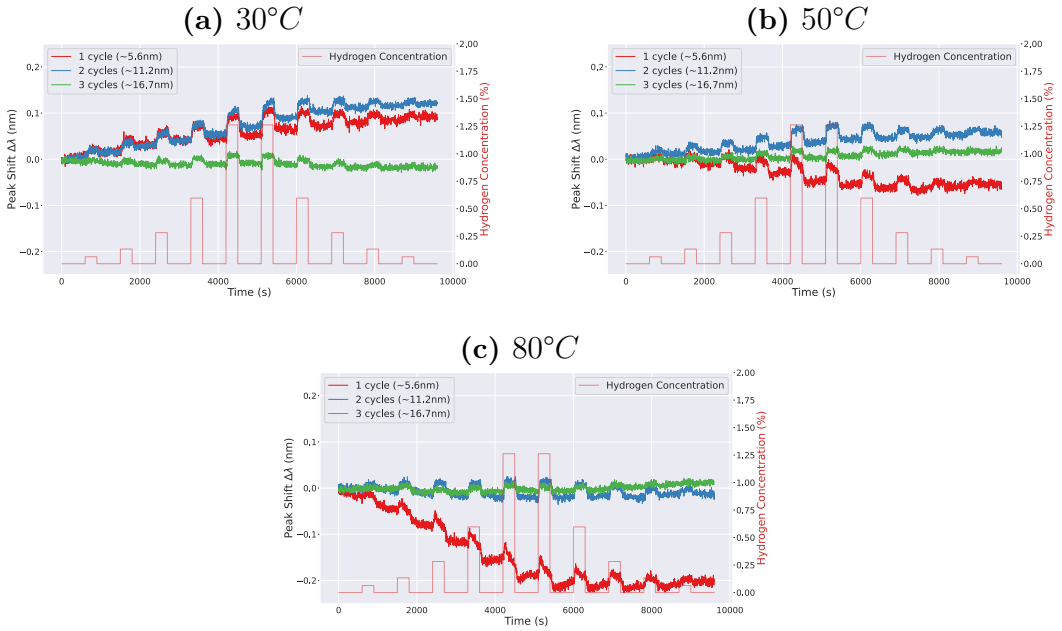

Figure 4.4: Peak shift $\Delta\lambda$ of 1 (5.6 nm), 2 (11.2 nm) and 3 (16.7 nm) cycles of PECVD SiN for each time step and centered on the hydrogen pulses at (a) 30°C, (b) 50°C and (c) 80°C. The thin layer (red) irreversibly blueshifts with increasing temperature.
Samples: 140x20 nm Ag, 1 - 3 cycles of PECVD SiN, 10 Å of Pd

Upon closer examination, the second observation one can make is that the thicker SiN layer provides a lower response compared to the intermediate thickness. This phenomenon can be explained as since the sensitivity of the Ag particles to changes in the surrounding environment decreases with distance, the Pd particles being located further from the silver antenna will have a lesser effect on the near-field of the Ag particle and thus provide a lower general response. This effect is evident when comparing the responses shown in Figure 4.5.

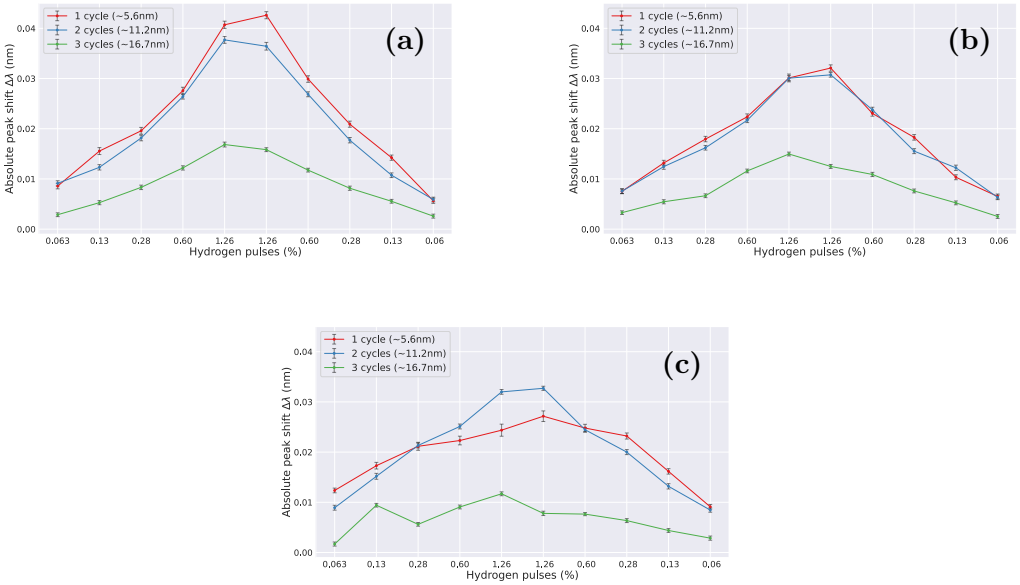

Figure 4.5: 1 (5.6 *nm*), 2 (11.2 *nm*), and 3 (16.7 *nm*) cycles of PECVD *SiN* exposed at (a) 30°*C*, (b) 50°*C*, and (c) 80°*C*. The thin layer (red) is unstable with increasing temperature, and the thick layer (green) has lower response than the thinner layers.
Samples: 140x20 *nm* Ag, 1 - 3 cycles of PECVD *SiN*, 10 Å of *Pd*

With an adequate *SiN* thickness, set at 2 cycles of *PECVD*, i.e., 11.2 *nm*, we can see that the temperature does not affect the sensor's response significantly, neither in magnitude nor in shape, as shown in Figure 4.6.

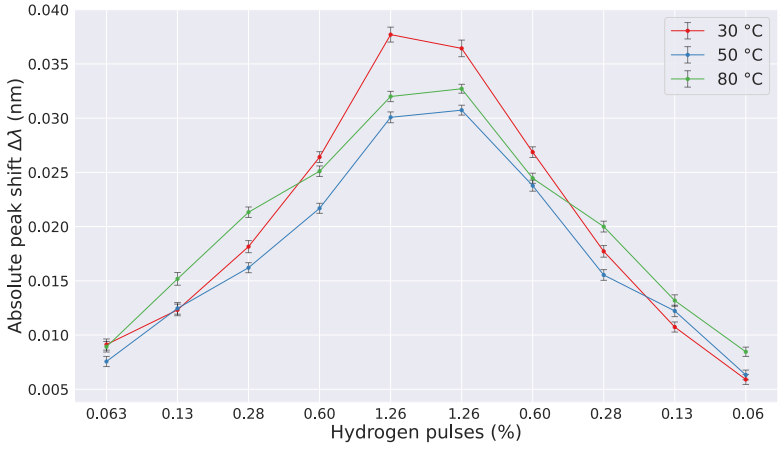

Figure 4.6: Peak shifts after different hydrogen pulses on 10 Å of *Pd* with 2 cycles (11.2 *nm*) of PECVD *SiN* at (red) 30°*C*, (blue) 50°*C* and (green) 80°*C*. Response is stable with increasing temperature.

However, using *PECVD* poses further issues when depositing through the mask, as

it could not consistently withstand temperatures of 170°C, which will be addressed in Section 4.3.

4.1.2 Influence of Pd nanoparticle sizes

The size of the Pd nanoparticles has a direct consequence on sensor response. Smaller particles are expected to exhibit faster hydrogenation kinetics due to their higher surface area-to-volume ratio, which facilitates quicker hydrogen adsorption and desorption processes. Conversely, larger particles tend to provide greater optical contrast, as each particle covers a larger area and therefore scatters more light. Top-view images of the different deposition thicknesses are shown in Figure 4.7. The thickness corresponds to the nominal value of Pd that has been deposited before dewetting, and a thicker layer is expected to produce larger particles after dewetting. From now on, all deposited thicknesses of Pd and $PdAu$ will be nominal.

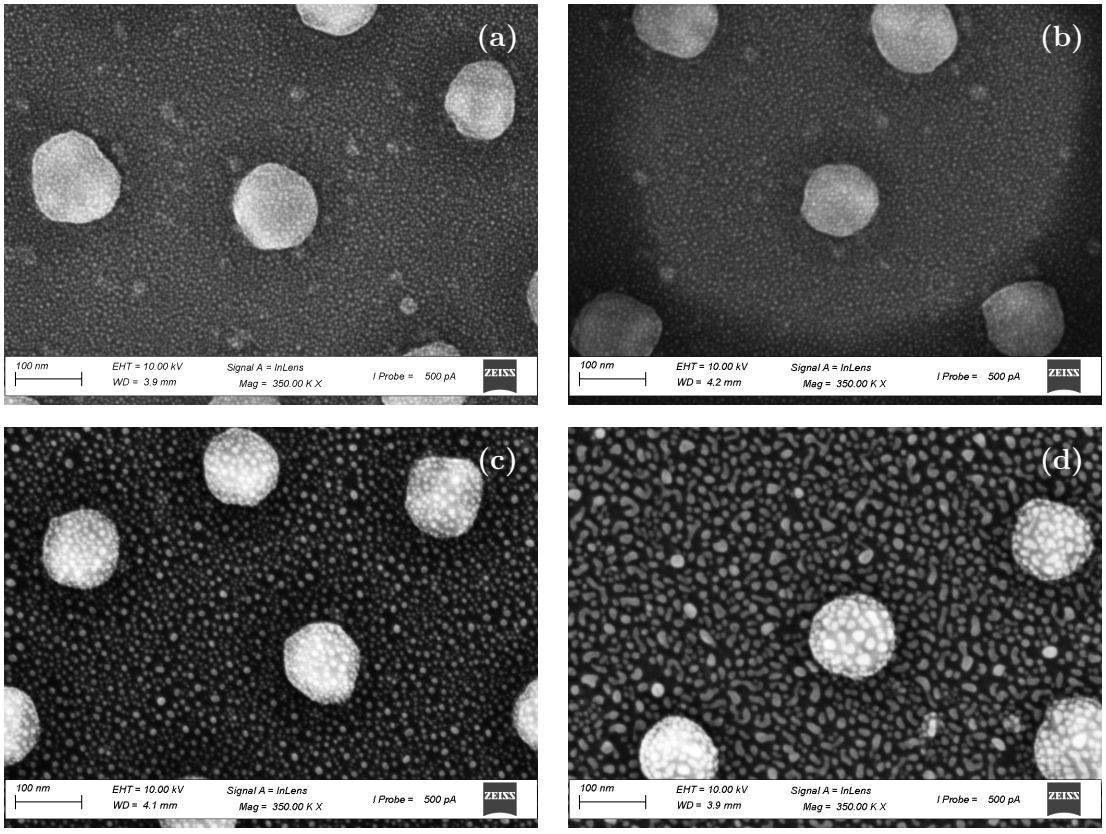

Figure 4.7: Top-view SEM images of Ag nanodisks $\simeq 140$ nm in diameter covered with small Pd nanoparticles. The different figures show how the Pd nanoparticle size and distribution vary with different nominal deposited thicknesses of (a) 3 Å, (b) 5 Å, (c) 10 Å and (d) 15 Å. Images were taken on a Zeiss Gemini 2.

The particle size statistics depending on the nominal deposited thickness of Pd are presented in Table 4.1 along with the images used for such analysis in Figure 4.8. The smallest deposition (3 Å) did not provide sufficient resolution in the SEM imaging to properly analyze the particle size, but indicated particle sizes around 5 nm and

below. Notably, the thickest deposition of 15 Å showed a large standard deviation, which is due to the fact that particle more poorly dewetted and formed elongated particles reaching up to 57.55 *nm* in Feret diameter.

Pd thickness [Å]	Mean [nm]	Std [nm]	Min [nm]	Max [nm]
3	< 5	/	/	/
5	4.99	2.29	1.16	11.97
10	7.06	3.05	1.47	15.5
15	16.43	10.15	2.34	57.55

Table 4.1: Particle feret ⌀ statistics as a function of nominal deposited thickness. The thinnest *Pd* thickness (3Å
did not provide satisfying images and was evaluated to have average size below 5 *nm*.

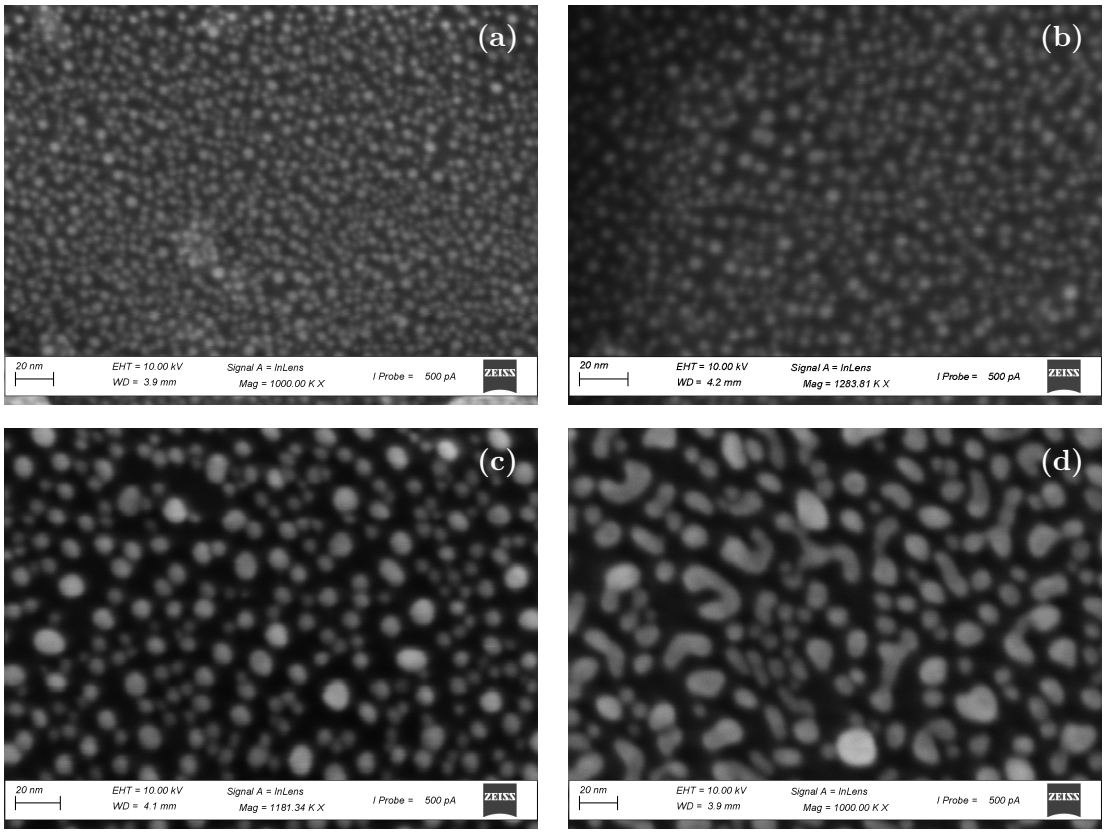

Figure 4.8: Top-view SEM images with high magnification of the small *Pd* nanoparticles. The different figures show how the particle sizes and distribution vary with different nominal deposited thicknesses of (a) 3 Å, (b) 5 Å, (c) 10 Å and (d) 15 Å. Note the difference in magnification (Mag=...). Images were taken on a Zeiss Gemini 2.

Finally, the combined peak shift performances of each evaluated thickness is presented in Figure 4.9. It can clearly be seen that there exist an optimum thickness

lying at 10 Å. This can be due to the fact that when the Pd layer gets too thick and covers more area, it changes the refractive index, thus shifting the resonance peak and interfering too much with the Ag particle own plasmonic resonance, reducing performances considerably.

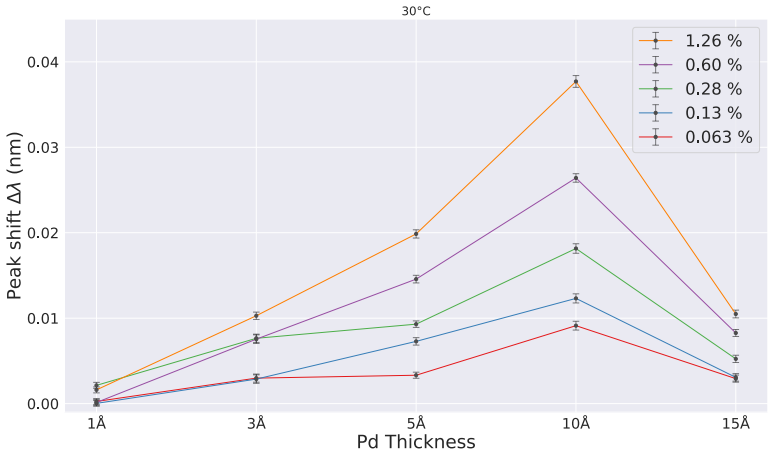

Figure 4.9: Change in centroid position for deposited Pd thicknesses ranging from 1 Å to 15 Å at 30°C. The different colors show each concentration of H_2 pulse that has been used.

4.2 Alloying of $PdAu$

4.2.1 Different layer depositions

In the case of $PdAu$ alloy, two different deposition methods have been investigated for each nominal thickness: whether Palladium or Gold was deposited first. Three different nominal thickness combinations have been used, keeping a composition ratio of $Pd_{70}Au_{30}$: 1 Å of Au with 3 Å of Pd, 3 Å of Au with 7 Å of Pd, and 6 Å of Au with 14 Å of Pd. The nomenclature used for indicating which element has been deposited first is $\frac{top\ layer}{bottom\ layer}$, i.e., 7Å of Pd deposited on top of 3Å of Au would be written $\frac{7Å\ Pd}{3Å\ Au}$.

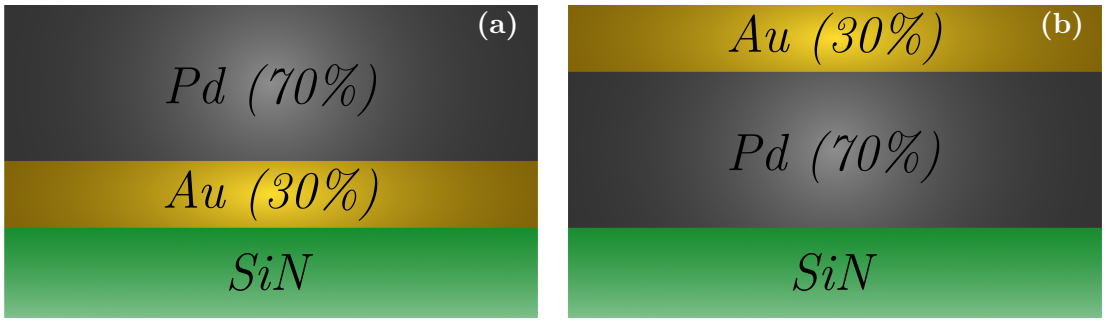

Figure 4.10: Visual representation of the two different PdAu deposition layouts used in this work. One material is deposited first onto the SiN protective layer, and the second layer is deposited afterward. Bear in mind that these are inhomogeneous films, due to the small scale and the deposition method (e-beam evaporation). The nomenclature used is (a): $\frac{70\%Pd}{30\%Au}$, (b): $\frac{30\%Au}{70\%Pd}$.

The order of the depositions proved to be much more important than originally expected. Indeed, analyzing the values reported in Table 4.2, we can see that the mean feret diameter of the particles is close to 4 times bigger when the Gold is deposited on top of the Palladium, and the size distribution is also larger, as shown with the larger relative standard deviation. This difference is likely due to the different wetting properties of Pd and Au with SiN, with Au known for having a higher surface diffusivity than Pd, leading to the formation of larger voids in the case where Pd is deposited first [33, 34]. These properties are linked to their surface and interfacial energies with SiN, which can be measured using Atomic Force Microscopy (AFM) or Focused Ion Beam (FIB) [35]. This difference in size unsurprisingly has had a significant impact on sensing performance. Indeed, the response results of $\frac{7\text{Å } Pd}{3\text{Å } Au}$ and $\frac{3\text{Å } Au}{7\text{Å } Pd}$ are shown in Figure 4.11.

Deposition order	Mean [nm]	Std [nm]	Min [nm]	Max [nm]
$\frac{7\text{Å } Pd}{3\text{Å } Au}$	3.275	0.996 (30.4%)	1.569	7.443
$\frac{3\text{Å } Au}{7\text{Å } Pd}$	11.815	5.739 (48.6%)	2.027	32.429

Table 4.2: Particle feret ⌀ statistics as a function of nominal deposited thickness

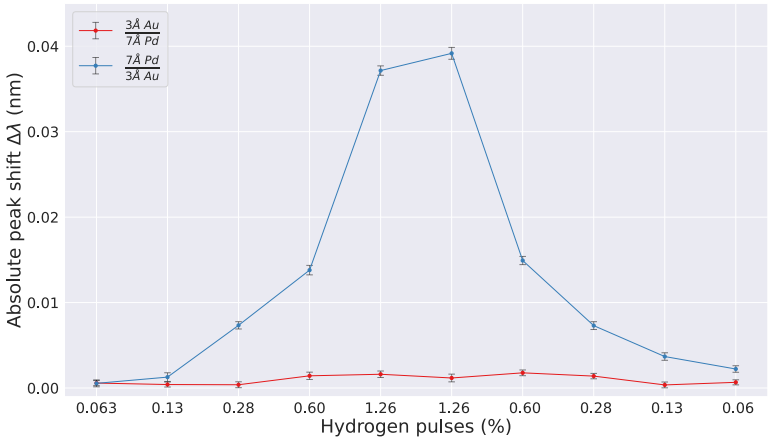

Figure 4.11: Peak shifts after different hydrogen pulses on (red) $\frac{7Å\ Pd}{3Å\ Au}$ (blue) $\frac{7Å\ Pd}{3Å\ Au}$ with 2 cycles (11.2 nm) of PECVD SiN at 30°C. Notice the significant difference in response. This is likely due to the different sizes shown in Table 4.2.

4.2.2 TEM composition imaging

A primary objective is to assess whether the particles have alloyed at all, or if each material has agglomerated on its own and formed a mixture of distinct Pd and Au particles, possibly of different sizes. TEM measurements were conducted to investigate such matter. In Figure 4.12, the EDX maps of b Au(M) and a Pd(L) show very similar areas of interest, indicating the presence of both Pd and Au in the same regions. Thus, we conclude that the particles have indeed alloyed.

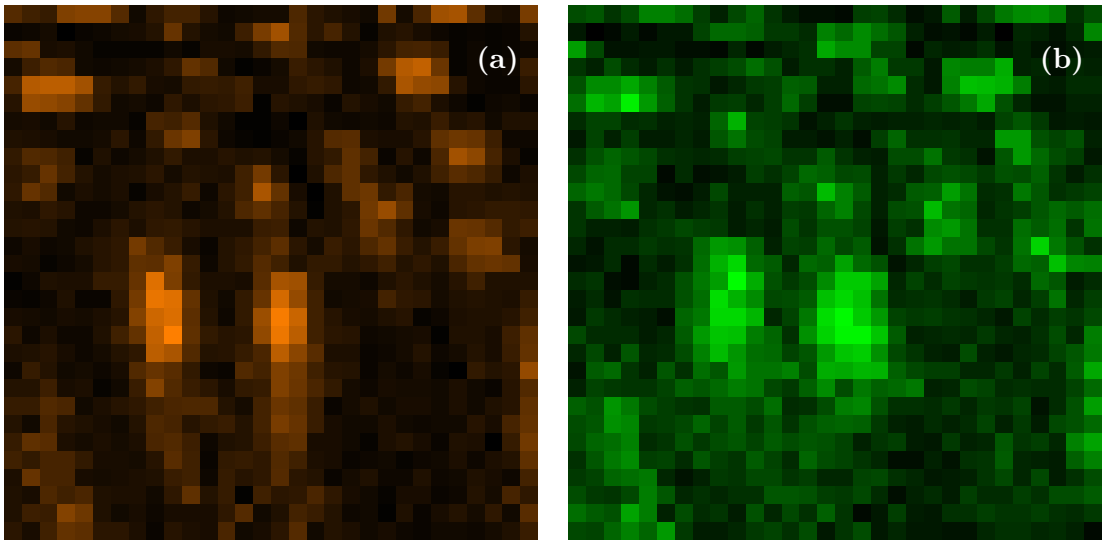

Figure 4.12: TEM EDX mapping of (a) Pd(L) and (b) Au(M). Images were taken on samples made specifically for TEM measurements with $\frac{7ÅPd}{3ÅAu}$ deposited on SiN.

Analyzing the compositions, several points have been found showing compositions

relatively close to the expected $Pd_{70}Au_{30}$. Albeit not exactly as hoped, these results remain encouraging considering the small scale and the measurements uncertainties. Compositions of three different points are reported in Table 4.3

	Element	Atomic %	Uncertainty %
Point 1	Pd(L)	87.89	12.75
	Au(M)	12.10	5.60
Point 2	Pd(L)	84.59	13.12
	Au(M)	15.40	5.85
Point 3	Pd(L)	80.80	8.56
	Au(M)	19.19	4.26

Table 4.3: TEM EDX quantification results of several points

Due to the very small scales at play, it proved challenging to obtain high-quality composition measurements. Nonetheless, these results indicate that at least some regions have alloyed. As shown in Table 4.3, there are several areas with presence of both Palladium and Gold in compositions relatively close to the expected 70% Pd and 30% Au. The overlap in the Au and Pd maps of Figure 4.12 further supports the alloying conclusion. Although preliminary, these findings suggest that the alloying process is effective. Further measurements on that topic could include longer TEM measurements or Atomic Probe Tomography.

4.2.3 Comparing with pure Pd

The best results for $PdAu$ were obtained with 14 Å of Pd deposited on top of 4 Å of Au. The combined thickness of Pd and Au is significantly higher than the best results obtained with pure Pd, at 10 Å. As shown in Table 4.2, the dewetting properties are greatly changed in this configuration, where Pd on top of Au leads to smaller particles than with the same total thickness if it were pure Pd. It is therefore not surprising that, to achieve same particle sizes with $PdAu$, the total thickness should be higher. One significant difference between the pure Pd samples and the alloyed $PdAu$, is that the first redshifts in presence of H_2, while the latter blueshifts. It has not been fully understood the reason for such behavior.

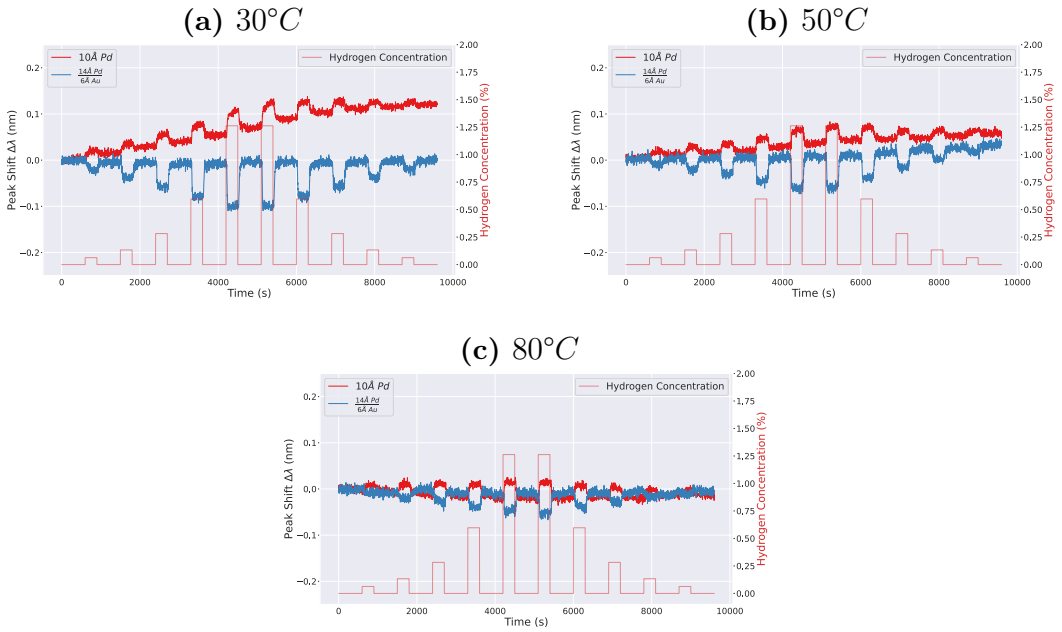

Figure 4.13: Peak shift $\Delta\lambda$ of (red) 10Å of Pd and (blue) $\frac{14ÅPd}{6ÅAu}$ with 11.2 nm of PECVD SiN for each time step exposed and centered on the hydrogen pulses at (a) 30°C, (b) 50°C, and (c) 80°C. See the difference in magnitudes between the pure Pd (red) and the $PdAu$ (blue). Especially at low temperature. Note that the responses differ in the sense that pure Pd induces a red shift in the response upon hydrogen exposition while $PdAu$ blueshifts.

Comparing the response magnitudes, $PdAu$ has a much greater performance, especially at low temperature (30°C), where it more than doubled the achieved response with pure Pd, as shown in Figure 4.14a. However, $PdAu$ is much more sensitive to temperature, and quickly goes down to similar performances than pure Pd at 80°C. A closer look on the influence of temperature on $PdAu$ is shown in Figure 4.15, where we clearly see the reduction in performance with increasing temperature.

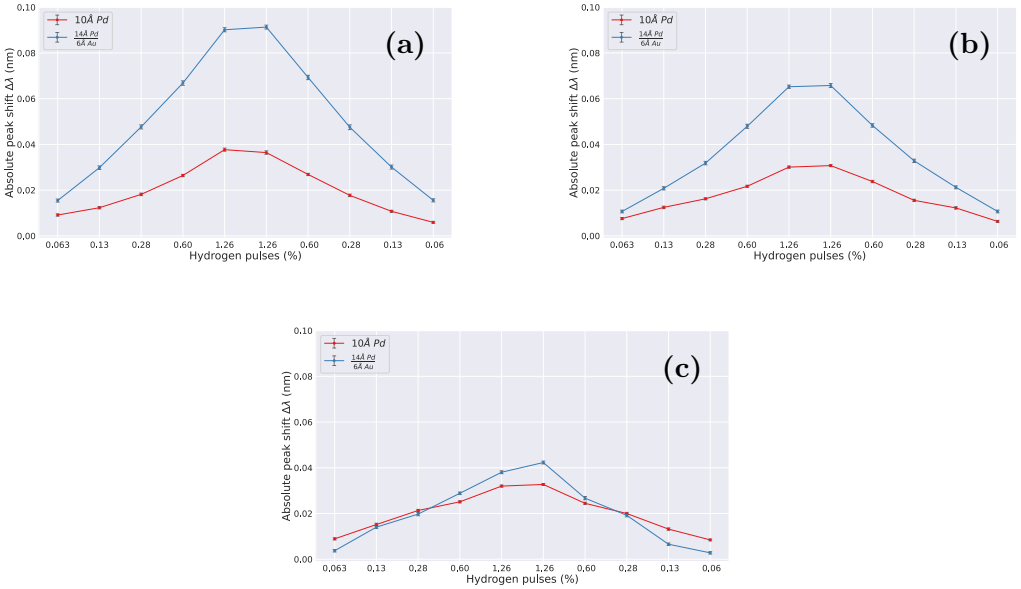

Figure 4.14: Absolute peak shift $\Delta\lambda$ of (red) 10Å of Pd and (blue) $\frac{14\text{Å}Pd}{6\text{Å}Au}$ with 11.2 nm of PECVD SiN for each hydrogen concentration exposed at (a) 30°C, (b) 50°C, and (c) 80°C. See the difference in magnitudes between the pure Pd (red) and the $PdAu$ (blue). Especially at low temperature. Note that the responses differ in the sense that pure Pd induces a red shift in the response upon hydrogen exposition while $PdAu$ blueshifts.

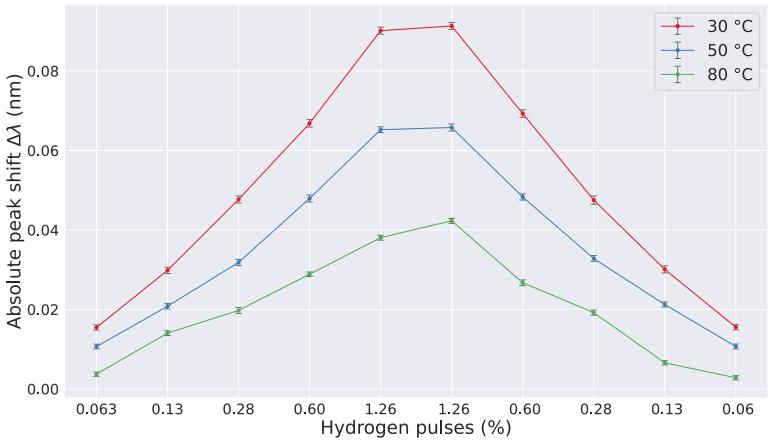

Figure 4.15: Peak shifts after different hydrogen pulses on 14 Å of Pd deposited on top of 6 Å of Au with 2 cycles (11.2 nm) of PECVD SiN at (red) 30°C, (blue) 50°C and (green) 80°C. The peak shift response greatly reduces with increasing temperature.

4.2.4 Kinetics of PdAu compared with its bulk equivalent

One of the motivations for using indirect LSPR is the use of rapid hydride forming particles, thus hopefully improving the kinetics of the system. To assess this result, we can compare the indirect method utilizing $PdAu$ alloy with its bulk, direct, equivalent. The latter is composed of 210 x 25 nm $Pd_{70}Au_{30}$ nanodisks. Comparing the responses using the Fast-Switch Mini Reactor developed by Iwan Darmadi during its PhD thesis [36], which allows for fast gas filling of the chamber, we see that the Ag indirect samples have much faster kinetics, as shown in Figure 4.16. The protocol was very similar than the one used in the X1 reactor except that the only temperature evaluated was 30°C. The response time is assessed by taking the mean value before and during the pulse, and extracting the time it takes to reach 90% of the difference between these two values. This time is called t_{90} and is a common way to evaluate sensor response. The direct method yielded around 28s to reach t_{90} while the direct method yielded 3s, which is around 10 times better and proves that indirect LSPR can be used as a means to improve kinetics.

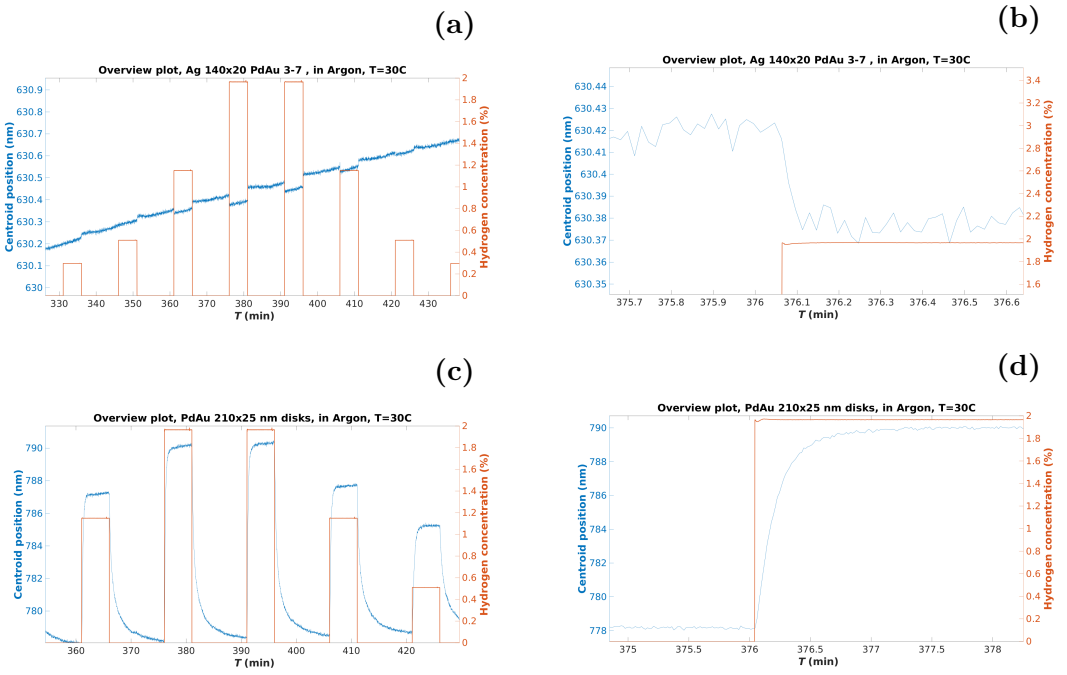

Figure 4.16: Side by side comparison of indirect and direct LSPR hydrogen sensing of $PdAu$ alloy at 30°C for kinetics analysis. (a) and (b) show the optical response of $\frac{7ÅPd}{3ÅAu}$, and (c) and (d) show the optical response of 210x25 nm $PdAu$ disks. Comparing (b) and(d), it can clearly be seen that the indirect method is much faster.

4.3 Through-Mask Pd Deposition

A last area of research from this thesis was to investigate Pd depositions through the mask, reducing the amount of Pd particles on the sample to the bare minimum.

This could further increase the rapidity of hydrogen intake, as there would not be any inactive Pd hydrogenation. There is a possibility that it would also change the dewetting process as each particle would have its own Pd thin film isolated from the others.

One area of concern in the current process is that the SiN is deposited at 300°C using PECVD. This temperature is much higher than what PMMA can withstand and the mask would collapse at such temperature. It has then been reduced to 170°C but still remained inconsistent and cracks occurred in the mask as shown in Figure 4.17, misaligning the Ag particles with the holes and making further depositions impossible. Furthermore, due to the excellent step coverage of PECVD, the SiN covers the sides of the holes and make the mask much harder to lift-off. Even after a full day in mr-Rem 700 (Microresist Technology GmbH) and another full day in Acetone, it was not properly lifted-off. Sonicator was then successively used for 5min in Remover, Acetone and Isopropanol, but the particles were severely damaged. It is likely due to the prolonged exposition to lift-off agents and perhaps also to the Sonicator. The damaged particles are shown in Figure 4.18

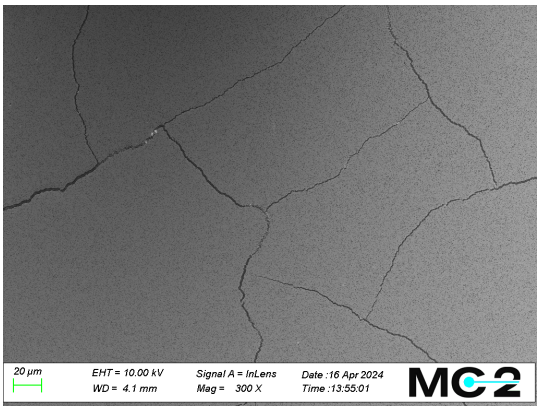

Figure 4.17: Top-view SEM image of the mask prior to lift-off. Cracks can be seen appearing in the mask after PECVD SiN deposition at 170°C.

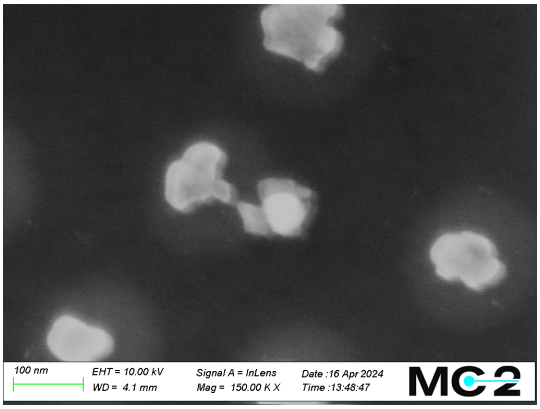

Figure 4.18: Top-view SEM image of a damaged Ag particle after PECVD SiN deposition at 170°C and long lift-off.

Despite unsuccessful, it can be concluded that a different process would be more suited for the purpose of depositing Pd through the mask. One good candidate is the use of a Cr hard sacrificial layer, as propose by Arturo Susarrey-Arce et al. [9], but it involves using hazardous chemicals for the Cr etching and has not been explored in this thesis. Another option would be to operate the $PECVD$ at even lower temperatures, although it could potentially compromise the quality of the SiN film and it has not been investigated in this thesis either.

5
Conclusion

The results from this Master's thesis project demonstrate that indirect LSPR can be effectively utilized for hydrogen sensing, offering improved kinetics compared to the direct bulk equivalent, particularly for $PdAu$ alloys.
The research highlighted the limitations of sputtered SiN for depositing the protective layer; therefore $PECVD$ is recommended for depositing the protective layer instead. It has been shown that a thinner protective layer enhances the response but makes the sensor more sensitive to temperature and may not efficiently protect against oxidation in ambient air when Ag plasmonic probes are used. Optimal Pd deposited thickness for nanoparticle formation through solid-state dewetting was found at 10Å, annealed at $500°C$ for $18H$. This yielded an average nanoparticle size of $7.06 \pm 3.05\ nm$. Furthermore and most interestingly, it has been shown that the formation of $PdAu$ nanoparticles through solid-state dewetting seems to be effective and provides twice better sensing performance than pure Pd, albeit with reduced thermal resistance. Its hydrogen sorption kinetics are significantly faster than the bulk equivalent in direct LSPR, showcasing a tenfold improvement. Additionally, it was observed that the order of depositions for $PdAu$ had a significant impact on the resulting particle size, likely due to the different wetting properties of Pd and Au with SiN. Depositing Au first resulted in smaller particles, whereas when Pd was first, particles were larger. For the sake of this experiment, depositing Au first resulted in better results.
Lastly, attempting to make all depositions through the mask at $170°C$ is not reliable due to the temperature sensitivity of $PMMA$. It has been suggested to update the process for a hard sacrificial layer instead, such as Cr.

6
Future work

The findings of this thesis open several pathways for further investigation, each with the potential to significantly enhance the performance and understanding of hydrogen sensors using LSPR.

1. **Optimization of working device**
   On one hand, improving the currently working devices could be done through investigating different annealing times and temperatures to refine nanoparticle size distribution and surface coverage. Additionally, finalizing the deposition through the mask would also likely improve performance, although it is unsure to what extent, as one reason for this approach is to minimize the amount of hydrogen absorbed by inactive Pd particles, but the required quantity of hydrogen is already very small. The impact of varying the size of Ag particles also presents an unexplored opportunity for improvement. A control experiment of Ag particles without SiN could be useful for understanding the phenomenon that happens when the SiN layer is very thin with increasing temperature. Faceting of the Pd particles could also be an interesting aspect to investigate [37].
2. **Advance alloying through solid-state dewetting**
   The promising results from alloying through solid-state dewetting of $PdAu$ suggest that more complex deposition layouts could yield further improvements. Longer TEM measurements are definitely required to better assess alloy compositions. Atomic Probe Tomography could also be an option to consider for that matter due to the small scales at play. Measurement of Pd/SiN_x interfacial energy could provide further insight on the solid state dewetting process, which can be achieved with AFM or FIB [35].
3. **Refine kinetic studies and isotherm analysis**
   More detailed kinetic studies are needed to understand the sensing dynamics fully. Investigating whether there is hysteresis in the isotherm responses of these materials would also add valuable data to the field.
4. **Theoretical understanding of spectral shift mechanisms**
   An unresolved question is the understanding of the mechanisms behind the observed redshift and blueshift in spectral responses between pure Pd and $PdAu$ alloy. Some Pd samples also exhibit blueshift and the reason has not yet been understood.

Bibliography

[1] J. O'M. Bockris. "A Hydrogen Economy". In: *Science* 176.4041 (1972), pp. 1323–1323. DOI: 10.1126/science.176.4041.1323. eprint: https://www.science.org/doi/pdf/10.1126/science.176.4041.1323. URL: https://www.science.org/doi/abs/10.1126/science.176.4041.1323.

[2] Jude A. Okolie et al. "Futuristic applications of hydrogen in energy, biorefining, aerospace, pharmaceuticals and metallurgy". In: *International Journal of Hydrogen Energy* 46.13 (2021), pp. 8885–8905. ISSN: 0360-3199. DOI: https://doi.org/10.1016/j.ijhydene.2021.01.014. URL: https://www.sciencedirect.com/science/article/pii/S0360319921000276.

[3] Pankaj Singh Chauhan and Shantanu Bhattacharya. "Hydrogen gas sensing methods, materials, and approach to achieve parts per billion level detection: A review". In: *International Journal of Hydrogen Energy* 44.47 (2019), pp. 26076–26099. ISSN: 0360-3199. DOI: https://doi.org/10.1016/j.ijhydene.2019.08.052. URL: https://www.sciencedirect.com/science/article/pii/S0360319919330034.

[4] Iwan Darmadi, Ferry Anggoro Ardy Nugroho, and Christoph Langhammer. "High-Performance Nanostructured Palladium-Based Hydrogen Sensors—Current Limitations and Strategies for Their Mitigation". In: *ACS Sensors* 5.11 (2020). PMID: 33181012, pp. 3306–3327. DOI: 10.1021/acssensors.0c02019. eprint: https://doi.org/10.1021/acssensors.0c02019. URL: https://doi.org/10.1021/acssensors.0c02019.

[5] Won-Tae Koo et al. "Chemiresistive Hydrogen Sensors: Fundamentals, Recent Advances, and Challenges". In: *ACS Nano* 14.11 (2020). PMID: 33124428, pp. 14284–14322. DOI: 10.1021/acsnano.0c05307. eprint: https://doi.org/10.1021/acsnano.0c05307. URL: https://doi.org/10.1021/acsnano.0c05307.

[6] Christoph Langhammer et al. "Indirect Nanoplasmonic Sensing: Ultrasensitive Experimental Platform for Nanomaterials Science and Optical Nanocalorimetry". In: *Nano Letters* 10.9 (2010). PMID: 20718400, pp. 3529–3538. DOI: 10.1021/nl101727b. eprint: https://doi.org/10.1021/nl101727b. URL: https://doi.org/10.1021/nl101727b.

[7] Christoph Langhammer et al. "Size-Dependent Kinetics of Hydriding and Dehydriding of Pd Nanoparticles". In: *Phys. Rev. Lett.* 104 (13 Mar. 2010), p. 135502. DOI: 10.1103/PhysRevLett.104.135502. URL: https://link.aps.org/doi/10.1103/PhysRevLett.104.135502.

[8] H. Fredriksson et al. "Hole–Mask Colloidal Lithography". In: *Advanced Materials* 19.23 (2007), pp. 4297–4302. DOI: https://doi.org/10.1002/adma.

200700680. eprint: https://onlinelibrary.wiley.com/doi/pdf/10.1002/adma.200700680. URL: https://onlinelibrary.wiley.com/doi/abs/10.1002/adma.200700680.

[9] Arturo Susarrey-Arce et al. "A nanofabricated plasmonic core–shell-nanoparticle library". In: *Nanoscale* 11 (44 2019), pp. 21207–21217. DOI: 10.1039/C9NR08097J. URL: http://dx.doi.org/10.1039/C9NR08097J.

[10] Gondia S. Seck et al. "Hydrogen and the decarbonization of the energy system in europe in 2050: A detailed model-based analysis". In: *Renewable and Sustainable Energy Reviews* 167 (2022), p. 112779. ISSN: 1364-0321. DOI: https://doi.org/10.1016/j.rser.2022.112779. URL: https://www.sciencedirect.com/science/article/pii/S1364032122006633.

[11] Sonal Singh et al. "Hydrogen: A sustainable fuel for future of the transport sector". In: *Renewable and Sustainable Energy Reviews* 51 (2015), pp. 623–633. ISSN: 1364-0321. DOI: https://doi.org/10.1016/j.rser.2015.06.040. URL: https://www.sciencedirect.com/science/article/pii/S1364032115006127.

[12] Hasan Muslemani et al. "Opportunities and challenges for decarbonizing steel production by creating markets for 'green steel' products". In: *Journal of Cleaner Production* 315 (2021), p. 128127. ISSN: 0959-6526. DOI: https://doi.org/10.1016/j.jclepro.2021.128127. URL: https://www.sciencedirect.com/science/article/pii/S0959652621023453.

[13] Wenguo Liu et al. "The production and application of hydrogen in steel industry". In: *International Journal of Hydrogen Energy* 46.17 (2021), pp. 10548–10569. ISSN: 0360-3199. DOI: https://doi.org/10.1016/j.ijhydene.2020.12.123. URL: https://www.sciencedirect.com/science/article/pii/S0360319920347376.

[14] National Aeronautics and Space Administration. *Safety Standard for Hydrogen and Hydrogen Systems: Guidelines for Hydrogen System Design, Materials Selection, Operations, Storage and Transportation*. Technical Memorandum NASA-TM-112540, NAS 1.15:112540, NSS-1740.16. Work of the US Government. Public use permitted. Headquarters: NASA, 1997. URL: https://ntrs.nasa.gov/api/citations/19970033338/downloads/19970033338.pdf.

[15] Michael Schwarzer et al. "Adsorption and Absorption Energies of Hydrogen with Palladium". In: *The Journal of Physical Chemistry C* 126.34 (2022), pp. 14500–14508. DOI: 10.1021/acs.jpcc.2c04567. eprint: https://doi.org/10.1021/acs.jpcc.2c04567. URL: https://doi.org/10.1021/acs.jpcc.2c04567.

[16] Carl Andersson. "Hydrogen sorption properties of Pd-based nanoparticles - the role of alloying and internal structure". Licentiate thesis. Chalmers University of Technology, 2024.

[17] F. D. Manchester, A. San-Martin, and John M. Pitre. "The H-Pd (hydrogen-palladium) System". In: *Journal of Phase Equilibria* 15 (1994), pp. 62–83. URL: https://api.semanticscholar.org/CorpusID:95343702.

[18] Herbert B. Callen. *Thermodynamics and an Introduction to Thermostatistics*. 2nd. John Wiley & Sons, 1985, p. 234.

[19] Nikonianman (Wikipedia contributor). *Au nanoparticles*. https://commons.wikimedia.org/wiki/File:Au_nanoparticles.jpg. Accessed: 09/06/24. 2015.

[20] Gustav Mie. "Beiträge zur Optik trüber Medien, speziell kolloidaler Metallösungen". In: *Annalen der Physik* 25 (1908), pp. 377–445.

[21] E. Hutter and J. H. Fendler. "Exploitation of Localized Surface Plasmon Resonance". In: *Advanced Materials* 16.19 (2004), pp. 1685–1706. DOI: https://doi.org/10.1002/adma.200400271. eprint: https://onlinelibrary.wiley.com/doi/pdf/10.1002/adma.200400271. URL: https://onlinelibrary.wiley.com/doi/abs/10.1002/adma.200400271.

[22] Christoph Langhammer et al. "Hydrogen Storage in Pd Nanodisks Characterized with a Novel Nanoplasmonic Sensing Scheme". In: *Nano Letters* 7.10 (2007). PMID: 17850168, pp. 3122–3127. DOI: 10.1021/nl071664a. eprint: https://doi.org/10.1021/nl071664a. URL: https://doi.org/10.1021/nl071664a.

[23] Carl Wadell et al. "Hysteresis-Free Nanoplasmonic Pd–Au Alloy Hydrogen Sensors". In: *Nano Letters* 15.5 (2015). PMID: 25915663, pp. 3563–3570. DOI: 10.1021/acs.nanolett.5b01053. eprint: https://doi.org/10.1021/acs.nanolett.5b01053. URL: https://doi.org/10.1021/acs.nanolett.5b01053.

[24] J. Spadavecchia et al. "Au Nanoparticles Prepared by Physical Method on Si and Sapphire Substrates for Biosensor Applications". In: *The Journal of Physical Chemistry B* 109.37 (2005). PMID: 16853216, pp. 17347–17349. DOI: 10.1021/jp053194j. eprint: https://doi.org/10.1021/jp053194j. URL: https://doi.org/10.1021/jp053194j.

[25] Claudia Manuela Müller and Ralph Spolenak. "Dewetting of Au and AuPt alloy films: A dewetting zone model". In: *Journal of Applied Physics* 113.9 (Mar. 2013), p. 094301. ISSN: 0021-8979. DOI: 10.1063/1.4794028. eprint: https://pubs.aip.org/aip/jap/article-pdf/doi/10.1063/1.4794028/13640910/094301_1_online.pdf. URL: https://doi.org/10.1063/1.4794028.

[26] F. A. Nugroho et al. "Metal–polymer hybrid nanomaterials for plasmonic ultrafast hydrogen detection". In: *Nature Materials* 18.5 (2019), pp. 489–495. DOI: https://doi.org/10.1038/s41563-019-0325-4. URL: https://www.nature.com/articles/s41563-019-0325-4.

[27] Andreas B. Dahlin, Jonas O. Tegenfeldt, and Fredrik Höök. "Improving the Instrumental Resolution of Sensors Based on Localized Surface Plasmon Resonance". In: *Analytical Chemistry* 78.13 (2006). PMID: 16808449, pp. 4416–4423. DOI: 10.1021/ac0601967. eprint: https://doi.org/10.1021/ac0601967. URL: https://doi.org/10.1021/ac0601967.

[28] Garet G Nenninger, Marek Piliarik, and Jirí Homola. "Data analysis for optical sensors based on spectroscopy of surface plasmons". In: *Measurement Science and Technology* 13.12 (Nov. 2002), p. 2038. DOI: 10.1088/0957-0233/13/12/332. URL: https://dx.doi.org/10.1088/0957-0233/13/12/332.

[29] L. R. Feret. Technical Report Group D, Volume 2. Zurich: Assoc. Internat. pour l'Essai des Mat., 1931.

[30] Henk G. Merkus. *Particle Size Measurements: Fundamentals, Practice, Quality*. Springer, 2009, pp. 15–. ISBN: 978-1-4020-9016-5. URL: https://link.springer.com/book/10.1007/978-1-4020-9016-5.

[31] Ming Hu et al. "The effects of nanoscaled amorphous Si and SiNx protective layers on the atomic oxygen resistant and tribological properties of Ag film". In: *Applied Surface Science* 258.15 (2012), pp. 5683–5688. ISSN: 0169-4332. DOI: https://doi.org/10.1016/j.apsusc.2012.02.062. URL: https://www.sciencedirect.com/science/article/pii/S0169433212002966.

[32] Y.J. Xu et al. "Preparation of novel SiO2 protected Ag thin films with high reflectivity by magnetron sputtering for solar front reflectors". In: *Solar Energy Materials and Solar Cells* 107 (2012), pp. 316–321. ISSN: 0927-0248. DOI: https://doi.org/10.1016/j.solmat.2012.07.002. URL: https://www.sciencedirect.com/science/article/pii/S0927024812003558.

[33] S. Kunwar et al. "Self-assembly of bimetallic auxpd1-x alloy nanoparticles via dewetting of bilayers through the systematic control of temperature, thickness, composition and stacking sequence". In: *Materials Research Express* 5.3 (2018), p. 035047. DOI: 10.1088/2053-1591/aab7ab. URL: https://doi.org/10.1088/2053-1591/aab7ab.

[34] L. Vitos et al. "The surface energy of metals". In: *Surface Science* 411.1 (1998), pp. 186–202. ISSN: 0039-6028. DOI: https://doi.org/10.1016/S0039-6028(98)00363-X. URL: https://www.sciencedirect.com/science/article/pii/S003960289800363X.

[35] Claudia Manuela Müller and Ralph Spolenak. "Determination of the Au/SiNx interfacial energy by AFM and FIB tomography". In: *Surface Science* 617 (2013), pp. 94–105. ISSN: 0039-6028. DOI: https://doi.org/10.1016/j.susc.2013.07.001. URL: https://www.sciencedirect.com/science/article/pii/S0039602813001921.

[36] Iwan Darmadi. "Polymer-Nanoparticle Hybrid Materials for Plasmonic Hydrogen Detection". PhD thesis. Chalmers University of Technology, 2021. ISBN: 978-91-7905-453-3.

[37] Arin S. Preston et al. "Dewetted nanostructures of gold, silver, copper, and palladium with enhanced faceting". In: *Acta Materialia* 165 (2019), pp. 15–25. ISSN: 1359-6454. DOI: https://doi.org/10.1016/j.actamat.2018.11.036. URL: https://www.sciencedirect.com/science/article/pii/S1359645418309121.

DEPARTMENT OF PHYSICS
CHALMERS UNIVERSITY OF TECHNOLOGY
Gothenburg, Sweden
www.chalmers.se

CHALMERS
UNIVERSITY OF TECHNOLOGY